



UNIVERSIDAD DE INVESTIGACIÓN DE TECNOLOGÍA EXPERIMENTAL YACHAY

Escuela de Ciencias Físicas y Nanotecnología

TÍTULO: Preliminary Study of the Angular Dependence on Light Detection Efficiency for the KM3NeT DOM

Trabajo de integración curricular presentado como requisito para
la obtención del título de Físico

Autor:

Mendoza Celorio Génesis Marisol

Tutor:

Ph.D. Yepes Ramírez Harold

Urququí, Junio 2020

SECRETARÍA GENERAL
(Vicerrectorado Académico/Cancillería)
ESCUELA DE CIENCIAS FÍSICAS Y NANOTECNOLOGÍA
CARRERA DE FÍSICA
ACTA DE DEFENSA No. UITEY-PHY-2020-00010-AD

A los 5 días del mes de junio de 2020, a las 17:00 horas, de manera virtual mediante videoconferencia, y ante el Tribunal Calificador, integrado por los docentes:

Presidente Tribunal de Defensa	Dr. COSENZA MICELI, MARIO GIUSEPPE , Ph.D.
Miembro No Tutor	Dr. SVOZILIK JIRI , Ph.D.
Tutor	Dr. YEPES RAMIREZ, HAROLD , Ph.D.

El(la) señor(ita) estudiante **MENDOZA CELORIO, GENESIS MARISOL**, con cédula de identidad No. **1315425064**, de la **ESCUELA DE CIENCIAS FÍSICAS Y NANOTECNOLOGÍA**, de la Carrera de **FÍSICA**, aprobada por el Consejo de Educación Superior (CES), mediante Resolución **RPC-SO-39-No.456-2014**, realiza a través de videoconferencia, la sustentación de su trabajo de titulación denominado: **Preliminary Study of the Angular Dependence on Light Detection Efficiency for the KM3Net DOM**, previa a la obtención del título de **FÍSICO/A**.

El citado trabajo de titulación, fue debidamente aprobado por el(los) docente(s):

Tutor	Dr. YEPES RAMIREZ, HAROLD , Ph.D.
--------------	-----------------------------------

Y recibió las observaciones de los otros miembros del Tribunal Calificador, las mismas que han sido incorporadas por el(la) estudiante.

Previamente cumplidos los requisitos legales y reglamentarios, el trabajo de titulación fue sustentado por el(la) estudiante y examinado por los miembros del Tribunal Calificador. Escuchada la sustentación del trabajo de titulación a través de videoconferencia, que integró la exposición de el(la) estudiante sobre el contenido de la misma y las preguntas formuladas por los miembros del Tribunal, se califica la sustentación del trabajo de titulación con las siguientes calificaciones:

Tipo	Docente	Calificación
Tutor	Dr. YEPES RAMIREZ, HAROLD , Ph.D.	9,8
Miembro Tribunal De Defensa	Dr. SVOZILIK JIRI , Ph.D.	9,1
Presidente Tribunal De Defensa	Dr. COSENZA MICELI, MARIO GIUSEPPE , Ph.D.	9,7

Lo que da un promedio de: **9.5 (Nueve punto Cinco)**, sobre 10 (diez), equivalente a: **APROBADO**

Para constancia de lo actuado, firman los miembros del Tribunal Calificador, el/la estudiante y el/la secretario ad-hoc.

Certifico que *en cumplimiento del Decreto Ejecutivo 1017 de 16 de marzo de 2020, la defensa de trabajo de titulación (o examen de grado modalidad teórico práctica) se realizó vía virtual, por lo que las firmas de los miembros del Tribunal de Defensa de Grado, constan en forma digital.*

MENDOZA CELORIO, GENESIS MARISOL
Estudiante

Dr. COSENZA MICELI, MARIO GIUSEPPE , Ph.D.
Presidente Tribunal de Defensa



Firmado electrónicamente por:
MARIO GIUSEPPE
COSENZA MICELI

Dr. YEPES RAMIREZ, HAROLD , Ph.D.
Tutor



Firmado electrónicamente por:
HAROLD
YEPES

Dr. SVOZILIK JIRI , Ph.D.
Miembro No Tutor

CIFUENTES TAFUR, EVELYN CAROLINA
Secretario Ad-hoc

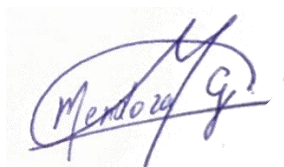


Firmado electrónicamente por:
EVELYN CAROLINA
CIFUENTES TAFUR

AUTORÍA

Yo, **GÉNESIS MARISOL MENDOZA CELORIO**, con cédula de identidad 1315425064, declaro que las ideas, juicios, valoraciones, interpretaciones, consultas bibliográficas, definiciones y conceptualizaciones expuestas en el presente trabajo; así como, los procedimientos y herramientas utilizadas en la investigación, son de absoluta responsabilidad de el/la autora (a) del trabajo de integración curricular. Así mismo, me acojo a los reglamentos internos de la Universidad de Investigación de Tecnología Experimental Yachay.

Urcuquí, julio 2020.

A handwritten signature in blue ink, appearing to read 'Mendoza G.', enclosed within a faint, light-colored oval or circular stamp.

Génesis Marisol Mendoza Celorio
CI: 1315425064

AUTORIZACIÓN DE PUBLICACIÓN

Yo, **GÉNESIS MARISOL MENDOZA CELORIO**, con cédula de identidad 1315425064, cedo a la Universidad de Investigación de Tecnología Experimental Yachay, los derechos de publicación de la presente obra, sin que deba haber un reconocimiento económico por este concepto. Declaro además que el texto del presente trabajo de titulación no podrá ser cedido a ninguna empresa editorial para su publicación u otros fines, sin contar previamente con la autorización escrita de la Universidad.

Asimismo, autorizo a la Universidad que realice la digitalización y publicación de este trabajo de integración curricular en el repositorio virtual, de conformidad a lo dispuesto en el Art. 144 de la Ley Orgánica de Educación Superior

Urcuquí, junio 2020.



Génesis Marisol Mendoza Celorio
CI: 1315425064

Dedicatoria

A mis padres, hermanos y sobrinos por su apoyo incondicional y fortaleza para cumplir mis metas.

Génesis Marisol Mendoza Celorio

Agradecimiento

En primer lugar, quiero expresar mi más sincero agradecimiento a mis padres Arturo y Rubiz, por apoyarme en todo momento durante mis años de estudio lejos de casa, por su confianza, por su amor y por su paciencia. A mis hermanos Karen, Kerly, Jonathan y Jordan por brindarme su apoyo incondicional durante mi carrera. A mis sobrinos Ainoha y Arturito por sus abrazos, besos y cariño sincero, son mi mayor motivación y este logro no hubiera sido posible sin ellos.

Quiero expresar mi agradecimiento a mi tutor de tesis Harold Yepes Ramírez por todo su tiempo y esfuerzo en mi trabajo de titulación. La puerta de la oficina del profesor Yepes siempre estaba abierta cuando me encontraba con un problema o tenía una pregunta sobre mi investigación o escritura. Le agradezco por todo el apoyo brindado, por las enseñanzas, correcciones, consejos y guías en este proyecto, enseñándome el camino de la investigación en la física de altas energías.

También agradezco a los expertos que estuvieron relacionados en este proyecto de investigación, al grupo de KM3NeT en Nikhef, especialmente a Paul de Jong, Ronald Bruijn, Thijs van Eeden, Brian Ó Fearraig and Lodewijk Nauta. Gracias por toda la ayuda, facilidades y conocimiento brindadas en el laboratorio, por la inspiración, las enseñanzas que me ayudaron durante mi estadía en Nikhef y en mi trabajo de investigación. Aprendí mucho en Ámsterdam durante los dos meses que estuve trabajando en Instituto Nacional Holandés de Física Subatómica en el “dark room”. Fue una experiencia extraordinaria de la cual quedo muy agradecida, que incluso en los coffee breaks aprendí a jugar fútbol con el grupo Nikhef-KM3NeT.

Me gustaría agradecer a la Escuela de Ciencias Físicas y Nanotecnología por el apoyo brindado durante la carrera, en especial la ayuda económica para hacer posible mi estadía de investigación en Ámsterdam, la cual fue parte esencial para mi proyecto de titulación. Gracias al decano y profesor PhD Ernesto Medina por la inspiración, apoyo y enseñanzas dentro y fuera del aula. Gracias a Evelyn Cifuentes, secretaria de la Escuela por su eficiencia, paciencia y amabilidad con los estudiantes. Un agradecimiento especial a todos los profesores que con sus enseñanzas han hecho posible que todos estos años de estudio y esfuerzo valgan la pena, gracias por motivarnos todos los días en el camino increíble de la investigación científica.

Quiero agradecer a mis compañeros de clase y ahora colegas por todas las clases, aventuras, madrugadas, noches de estudio, celebraciones y más que vivimos durante estos años. Me gustaría agradecer a mis queridos amigos Evelyn Mollocana, Carla Borja, Kabir Sulca y Daniela Montalvo por su amistad, apoyo incondicional en todo momento y aventuras compartidas. Un agradecimiento especial a mis roommates, tía Naiden, Viko, Mary, Tivo y JD por su compañía, noches de risas, cenas, viajes y amistad, haciendo la estadía en la universidad mucho más comfortable.

Finalmente, le agradezco especialmente a Juan David Alcívar por su ayuda en este trabajo. Durante 4 años se ha convertido en mi compañero de estudio, de negocios, de viajes y aventuras, mi mejor amigo y mi apoyo incondicional. Gracias por todo el amor, tiempo, paciencia y motivación que me das, siempre estaré agradecida con tu compañía, alegría y enseñanzas.

Génesis Marisol Mendoza Celorio

Resumen

KM3NeT es una colaboración internacional que está construyendo un observatorio de neutrinos a escala km³ que se está desplegando en el mar Mediterráneo. El observatorio utiliza la misma tecnología en dos sitios diferentes, con los detectores ARCA y ORCA, implementando detectores a gran escala para el estudio del flujo de neutrinos de alta energía y la determinación de la jerarquía de masa de neutrinos, pero también permite estudios para las Ciencias de la Tierra y las Ciencias del Mar. Los detectores están formados por grandes conjuntos de miles de sensores ópticos capaces de detectar la luz de Cherenkov inducida por la interacción de los leptones con el medio. Dichos arreglos consisten en líneas verticales llamadas Unidades de Detección (DU) que contienen 18 módulos ópticos digitales (DOM). El DOM es una esfera de vidrio de 17 pulgadas que es resistente a la presión y alberga los 31 tubos fotomultiplicadores de 3 pulgadas (PMT) que son el sensor óptico. El principio de funcionamiento de los PMT se basa en el efecto fotoeléctrico externo, donde los fotones golpean un fotocátodo en la ventana de entrada y produce electrones por emisión secundaria. El propósito de esta investigación experimental es estudiar la respuesta de PMT en términos de eficiencia, aceptación angular y tamaño de la señal. Estas propiedades se estudian con la ayuda de una configuración que consiste en un DOM dentro de un "acuario" lleno de agua, buscando emular las condiciones de operación de cerca. Los resultados de este estudio han proporcionado una mejor comprensión del comportamiento de los PMT que juegan un papel crucial en la reconstrucción del evento en KM3NeT, la detección de neutrinos y, por lo tanto, en el éxito de sus programas de ciencias.

Palabras Clave: KM3NeT, Luz Cherenkov, PMT, aceptación angular, eficiencia

Abstract

KM3NeT is an international collaboration constructing a km³-scale neutrino observatory being deployed at the Mediterranean Sea. The observatory uses the same technology in two different sites, detectors ARCA and ORCA, implementing large-scale detectors for the study of the high-energy neutrino flux and the determination of the neutrino mass ordering, but also with ports for the Earth and Sea Science. Detectors are made of large arrays of thousands of optical sensors able to detect the Cherenkov light induced by the interaction of leptons with the medium. Such arrays consist of vertical lines called Detection Units (DU) containing 18 Digital Optical Modules (DOMs). The DOM is a 17-inches glass sphere which is pressure-resistant and houses the 31 3-inches Photomultiplier Tubes (PMTs) which are the optical sensor. The operating principle of PMTs is based on the external photoelectric effect, where photons strike a photocathode at the entrance window and produce electrons by secondary emission. The purpose of this experimental research is to study the response of PMT in terms of efficiency, angular acceptance, and size of the signal. These properties are studied with the help of a setup consisting of a DOM inside of an "aquarium" filled with water, looking to emulate the operation conditions closely. The results from this study have provided a better understanding of the behavior of PMTs that play a crucial role in the KM3NeT event reconstruction, neutrino detection, and hence, in the success of its science programs.

Palabras Clave: KM3NeT, Cherenkov light, PMT, angular acceptance, efficiency

Contents

List of Figures	viii
List of Tables	xii
List of Papers	xiii
1 Introduction	1
1.1 Problem Statement	3
1.2 General and Specific Objectives	3
2 Cosmic Rays and Neutrino Physics	5
2.1 Cosmic Rays	5
2.2 Neutrinos	7
2.3 Neutrino interactions	7
2.4 Neutrino oscillation	8
2.4.1 Mixing of neutrino eigenstates and oscillation parameters	9
2.4.2 Neutrino Mass Hierarchy (NMH)	10
2.5 Neutrino Sources	10
2.5.1 Extra-galactic origin	11
2.5.2 Galactic origin	12
2.5.3 Other neutrino sources	12
3 The KM3NeT Neutrino Telescope	13
3.1 Cherenkov radiation and propagation	13
3.2 Detector Design	15
3.2.1 The Digital Optical Module (DOM)	15
3.2.2 Detection Unit (DU)	16
3.2.3 Building Blocks (BB)	17
3.3 Background sources	18

3.3.1	The optical background	18
3.3.2	The physical background	19
4	Photomultiplier Tubes	21
4.1	Properties of Photomultiplier Tubes (PMTs)	21
4.2	KM3NeT PMT requirements	22
5	Methodology	27
5.1	Experimental setup (test bench)	27
5.1.1	Laser setup	28
5.1.2	Photomultiplier Tube (PMT) calibration	29
5.1.3	Data acquisition	30
5.2	Data taking routines	31
5.2.1	Angular dependence on detection efficiency	31
5.2.2	Symmetry response to light detection	32
6	Results and Discussion	35
6.1	PMT scanning: angular dependence on light detection efficiency	35
6.1.1	PMT scanning: 180° laser-PMT	35
6.1.2	PMT Scanning: 150° laser-PMT	40
6.1.3	PMT Scanning: 120° laser-PMT	41
6.1.4	PMT Scanning: 90° laser-PMT	42
6.2	Symmetry response on light detection efficiency	43
6.3	Symmetry scanning results	44
6.4	Timing information: ToT distribution	46
6.5	Timing information: arrival time distribution	46
6.6	Data availability and reproducibility issues	48
7	Conclusions and Future Work	49
	Bibliography	51
	Abbreviations	55

List of Figures

2.1	Cosmic Ray energy spectrum: Global view of the cosmic ray range of energy spectrum. All data are recollected for several experiments as indicated	6
2.2	Standard Model of Elementary Particle. Summary and classification of all elementary particles forming the building blocks of matter.	8
2.3	Neutrino interaction cross section as a function of energy. Neutrino interaction cross section scales as a function of energy, the range of energy gives some sources of neutrinos are also illustrated.	9
2.4	Neutrino interaction channels. a) Neutral Current that results as hadronic cascade and an invisible outgoing neutrino. b) Charged Current of electron neutrinos that produce an electron and instantaneously an electromagnetic cascade. c) Charged Current Muon neutrino that produces hadronic cascade and a muon and d) Charged Current tau neutrino that produces a hadronic shower and a tau, tau decays fast and produce an additional hadronic or electron cascade.	10
2.5	Scheme of NMH. Each neutrino flavor is represented by a color. Normal and Inverted Hierarchy representations are shown.	11
3.1	The KM3NeT DOM. A DOM consists of a glass spherical vessel, 31 PMTs arranged to look in all directions, LED, CLB, PB, associated readout, power supply and communication.	15
3.2	Main electronics boards of the DOM. a) Central Logic Board (CLB). b) PMT base mounted. . . .	16
3.3	Scheme of 115 Detection Unit (DU) forming a Building Block (BB). It is a representation of what is expected to be fully operating at the abyssal sites of KM3NeT once completed. BB describes the complex structure and distances for ORCA/ARCA. A close view of a DU with buoys and anchor dead weight is represented, additionally, it shows how two ropes connect the DOMs.	17
3.4	Building Blocks in KM3NeT. ARCA consist of 2 BBs and ORCA just one. This illustration compares the difference of the scales, function of their scientific goals.	18
4.1	Scheme of the working principle of a PMT. A photon hits the photo-cathode and produce an electron, the electron is focused to the first dynode, where the electron starts a multiplication process by the emission of secondary electrons, this is repeated until the last dynode to arrive at the anode, and readout.	22

4.2	Pictures of PMT used in KM3NeT: a) Picture of a side view of the PMT with the electronic base. b) Picture of the top view of the PMT. The design of the PMT is crucial to reach KM3NeT scientific challenges	23
4.3	Scheme of the geometry of the reflection ring. Each PMT inside the DOM is surrounded by an reflector ring that was designed to improve the detection of light, it allows that of light coming perpendicular to the PMT will be collected by reflection sending to the photocathode in order to do not loss the photon.	23
4.4	Properties of Hamamatsu PMT R12199-02. a) Relation between analogue Voltage vs Time (dashed lines) and ToT (solid lines) signals from the KM3NeT PMT base. b) Typical ToT distribution showing the fit to the peak whose value corresponds to 26.4 ns as required by KM3NeT.	24
5.1	Setup for light detection efficiency studies. A) Dark box of blue color on the left, it is containing the aquarium with a Digital Optical Module (DOM) inside and the collimator. B) It is the pulse generator and the control of electronics of the DOM. C) It is an external CLB used for calibration and triggering the laser D) is the laser driver.	28
5.2	Dark Box. Left: the dark box used for the experiment. It can be open from one side and the top. The aquarium and the laser collimator are inside. Right: the DOM inside the aquarium. DOM is in rotatory support. The support avoids DOM floating using weights. In front of the DOM is the pulsed collimator laser in a rail that moves in x and z directions	29
5.3	Scheme of the top view of the movable DOM and laser setup. It is a scheme of the available choices for study at several angles the light detection efficiency. Left the PMT in front of the laser at $\theta = 180$. Right after moving the laser and rotate the DOM by 30°	30
5.4	Scheme of the laser setup. The use of White Rabbit Switch (WRS) guarantees absolute synchronization of time, which the DOM and the external CLB are connected through. This diagram shows the laser driver connected to the external CLB to control laser trigger.	31
5.5	PMT mounting frame. Left: The PMT close to the titanium collar is marked with a red point for reference. The collimator is on the rails in front of the PMT. Right: Close view of the titanium collar and vertical support.	32
5.6	Data points scanning. Left: the PMT selected closed to the titanium collar. Right: the representation of the 4 diagonals, where each black dots are measurement data. The picture was made through the glass and water.	33
5.7	Light source(laser)-light sensor(PMT) orientations for angular dependence studies. Measurements were taken in four different position of the DOM for the same PMT as figure suggests for scanning Detection Efficiency (DE).	33
5.8	Light source (laser)-light sensor (PMT) orientations for symmetry response studies. Measurements were taken at 3 different position of the DOM for the same PMT. Mostly the same points were taking at the opposite angles to observe variations in PMT response.	34

6.1	Location of the DOM at 180°. Left: picture of the whole DOM inside the aquarium. Right: view from the line of sight of the laser. The angle between the laser and the optical axis is 180°	36
6.2	Efficiency heat map at $\theta = 180^\circ$ (first trials). Left: first plot is not well defined, PMT and reflector ring are not clearly visible. Right: details around the PMT and reflector ring get improved because large statistics on data taking is considered.	37
6.3	Efficiency heat map at $\theta = 180^\circ$ (optimized by interpolation). The diagonals data points are illustrated, the plot also shows the optimized linear interpolated result. The inner ring represents the PMT and the outer ring the edge of the reflector ring.	37
6.4	Relative output of the Hamamatsu PMT. Left-Center. Two plots of the relative output of a PMT, where the horizontal and vertical axis of the photocathode were scanned with different wavelengths. Both plots present non uniformity along both axis with dynodes. Right: Top view of a Hamamatsu PMT, first and second dynode are seen with reference lines for scanning at x-y axis. The uniformity varies over the surface of the photocathode.	38
6.5	Projection of efficiency points. Top: PMT scanning at 180° , different PMT of the same DOM, dynodes position represented the first dynode in blue and second dynode in green. Black line represents points projected in the efficiency plot and red dashed lines the edge between the PMT and reflector ring. Bottom: projection plot of efficiency at 180° for the PMT at x position.	39
6.6	Detection Efficiency for the Hamamatsu PMT. a) Comparison between PMT efficiency measurements taken from Erlangen and Nikhef (this work). b) Data from Nikhef scaled by a factor of 2.	40
6.7	Location of the DOM at 150°. Left: picture of the whole DOM inside the aquarium 30° rotated. Right: view from the line of sight of the laser. The angle between the laser and the optical axis is 150°	41
6.8	Efficiency heat map at $\theta = 150^\circ$ (optimized by interpolation). Diagonals data points are illustrated, the plot also shows the optimized linear interpolated result. The efficiency is relatively higher on the right side at (-140, 235) position, the separation of the reflector ring is not clear enough.	41
6.9	Location of the DOM at 120°. Left: picture of the whole DOM inside the aquarium rotated another 30° . Right: view from the line of sight of the laser. Now the angle between the laser and the optical axis is 120° . The vertical supports starts to block the PMT.	42
6.10	Efficiency heat map at $\theta = 120^\circ$ (optimized by interpolation). Diagonals data points are illustrated showing the linear interpolated result. The efficiency is relative higher on the vertical diagonal, and the separation of the reflector ring is not clear. The influence of the vertical support is seen as blocking the view of the PMT.	42
6.11	Location of the DOM at 90°. Picture of the whole DOM inside the aquarium rotated another 30° . Now the angle between the PMT and the laser is 90° . The view of the PMT from the laser is totally blocked by the vertical support.	43

6.12	Efficiency heat map at $\theta = 90^\circ$ (optimized by interpolation). Diagonals data points are illustrated showing the linear interpolated result. The efficiency is relative "higher" on the vertical diagonal, and the separation of the reflector ring is not clear. The vertical support was totally blocking the view of the PMT.	43
6.13	Relative acceptance vs $\cos(\theta)$ for a KM3NeT DOM. The experimental measurements shown are obtained from each heat map (optimized by interpolation) and integrating over the scanned surface obtaining a normalised relative acceptance plot. The blue line corresponds to the latest KM3NeT OMGsim v2.0 Monte Carlo.	44
6.14	Efficiency scanning plots used to study symmetries in PMTs (optimized by interpolation). The plots compare the heat maps at 3 different angles. When the PMT is fixed at $\theta = 180^\circ$, next angles are rotating 30° to right and 30° to left, as a mirror-like projection.	45
6.15	Symmetry relations between heat maps (optimized by interpolation). Two heat maps on the top are for $\theta = [210^\circ, 150^\circ]$. In order to compare the heat maps at 150° the x coordinates were flipped and the heat map for $\theta = 210^\circ$ is kept without flipping.	45
6.16	ToT distributions of three different points in the PMT. Left: ToT distribution comparison, at different position. Right: Corresponding heat map of the ToT distribution in the PMT shows three color points represented in the distribution at left.	47
6.17	Arrival time distribution and heat map for PMTs. Left: three points in the PMT were studied through the arrival time distribution. Right: heat map for arrival time distribution. The range of arrival time distribution goes from $[220, 226]$ ns in the PMT.	47

List of Tables

4.1	Main requirements for the 3-inch PMT performance in KM3NeT	22
-----	--	----

Chapter 1

Introduction

The most exciting phrase to hear in science, the one that heralds new discoveries, is not "Eureka" but "That is funny . . ."
-ISAAC ASIMOV

At present, the development of technologies and tools to study the universe are moving at significant steps. The attempt to look beyond has achieved great discoveries. In modern physics, there still exists a lot of information unknown, but it is impressive how fast, extend our knowledge about the universe and its content has become. Astronomical science and engineering have allowed to discovered signals that for the naked eye were invisible, with specific and sophisticated instruments used to record and analyze the information reaching us from galaxies, stars or other astrophysical sources. Until recent times, most of the information and knowledge about the universe has almost exclusively extracted from photons, through wide ranges of energy, x-rays, γ rays, and others as radio.

However, due to some constraints using photons in the study of distant and dense astrophysical sources, because of absorption by interstellar media, they cannot carry the information on the arrival direction in regions opaque to photons. Other particles reach us and astronomy is taking advantage of these messengers particles to study different regions of the universe in exotic ways. One kind of those particles are fast-moving charged particles that arrived evenly from all directions of the sky and travel nearly to the speed of light; they are high energy protons and nuclei called Cosmic Rays (CRs). Charged particles, whose paths are deflected by magnetic fields, they cannot carry the information on the arrival direction up to Very-High Energy (VHE) and Ultra-High Energy (UHE). With the discovery of these particles new questions arise, i.e. "where do they come from?" and "how do they accelerate to reach such high energies?", actually with not sufficient answers, mainly because interstellar magnetic fields altered their trajectories. However, it is possible to "see" what correct cosmic ray sources are not able to, by using two uncharged high-energy messengers: γ rays and neutrinos, which are helping to tackle this challenge.

Photons, CRs, neutrinos and gravitational waves are considered a promising field of research as multi-messenger

astronomy in which photons, VHE and UHE nuclei are not only the probes with the extended information carried by neutrinos and gravitational waves. So, that a close look at production and acceleration sites of cosmic rays is only possible with neutral and weakly interacting messengers. Photons have an even larger probability than protons to be absorbed by the microwave background photons or interstellar material. The universe is not empty but filled with Cosmic Microwave Background (CMB)¹. CMB is the radiation left over from the Big Bang. In this way, high-energy astronomy makes use of the features of multi-messengers to understand and explore the most violent phenomena and extreme conditions in the universe. Astronomical observatories are called to form as a global events alert system, providing access to cosmic probes such as LIGO/VIRGO for gravitational waves, HESS/Fermi for photons, MYTHEN for single photon counting mode, AUGER for CRs and IceCube/KM3NeT for neutrinos, only to name a few.

In the last years, scientists have turned their attention to neutrinos. They are chargeless leptonic particles, and they are only weakly interacting, not deflected neither absorbed and have a small cross-section for the interaction with other particles. Neutrinos are postulated as the best tool for looking to sources of cosmic rays either galactic and extragalactic origin. On the other hand, the unique properties of neutrinos make them hard to detect. Due to the small cross-section, a large detector is needed. When neutrinos interact with a medium as seawater (dielectric medium), it creates charged particles (leptons), inducing Cherenkov light radiation, since leptons are released at a velocity greater than the group velocity of light in the medium. Developing a light detector into these media allows to indirectly detect neutrinos in a vast energy range (GeV to EeV), depending on the layout and design. KM3NeT is an international collaboration, operating a large research infrastructure housing the next generation large scale neutrino "telescopes"² under construction in the abyss of the Mediterranean Sea.

KM3NeT is composed of large arrays of thousands of optical sensors (PMTs) able to detect the Cherenkov light induced by the neutrino interactions in the seawater with nucleus produced a lepton of the same flavor. The two main objectives of the collaboration are the discovery of high-energy neutrino sources in our universe and the determination of the neutrino mass hierarchy. In order to achieve its scientific goals, a proper design, calibration and operation must be implemented into two kind of detectors with the same technology but at different scale, Astroparticles Research with Cosmics in the Abyss (ARCA) and Oscillation Research with Cosmics in the Abyss (ORCA). ARCA and ORCA use PMTs as the first frontier in photo-detection. In this complex device, an electrical signal is processed and treated, then, the information about neutrino origin and energy can be inferred from position, timing and amount of Cherenkov light reaching the PMTs.

PMTs are commonly used as detectors for high-energy physics experiments. Among some examples of the use of PMT in high-energy physics are collider astroparticles or experiments, where PMTs are used in hodoscopes, calorimeters, TOF counters, and Cherenkov counters. Beside high-energy physics experiments, there are many other uses for PMTs, in which Ecuador might be interested to explore beyond. Among some areas of interest, there are spectrophotometry, medical equipment, and biotechnology. In spectrophotometry, the principle is to study materials or substances in the function of transmission and reflection of light properties. Some applications are tests

for analyzing the presence of drugs or specific components in a sample. In the case of medical equipment, PMTs are part of imaging devices. Some examples are Position Emission Tomography (PET), gamma cameras, X-ray equipment, in-vitro assay, and many more. These devices can provide images of the living body and allow early diagnosis of lesions and tumors. For biotechnology, major equipment is used for life science which includes cell sorters, fluorimeters and DNA sequencers. Although Ecuador has extremely reduced activities around PMT science and technology, it does not look so crazy if we think about its regular use in the detection of drugs, medical purposes and other applied applications towards Ecuador gross domestic product contribution.

1.1 Problem Statement

KM3NeT is a network of deep-sea neutrino telescopes in the Mediterranean Sea with user ports for Earth and Sea sciences. The study of the identification and properties of cosmic neutrinos can provide the opportunity to identify galactic and extra-galactic sources, and solve the puzzle of the Standard Model of particle physics and beyond. This research thesis is a preliminary study of the Detection Efficiency (DE), angular acceptance inference and timing features of Photomultiplier Tubes (PMTs) with data measured at Nikhef laboratory at the Netherlands. A particular motivation of learning about PMTs technology on applications in the Ecuadorian context is an added value of this research.

1.2 General and Specific Objectives

General Objective:

Study some features of PMTs and understand its behaviour, and feedback calibration analysis and simulation inputs for KM3NeT, and set a precedent as technology with lots of applications into the Ecuadorian context linked to the "*Plan Nacional de Desarrollo*".

Specific Objectives:

Understand and analyze efficiencies, angular acceptance, timing features and symmetry patterns as a response facing a pulsed light source (laser), in the context of KM3NeT activities. It covers:

- Development of programming skills in ROOT, C++ and Python as frontier programming languages in subatomic physics.
- PMTs laser scanning in order to obtain detection efficiency plots.
- Study angular acceptance at specific points in the PMT and compare response at different angles.
- Study position dependence and symmetries in PMTs comparing and providing feedback for calibrations and simulations of the DOM.

- Compare relative acceptance plots with official simulations of KM3NeT.
- Study timing features related to the arrival time of photons and ToT of PMTs.

Chapter 2

Cosmic Rays and Neutrino Physics

This chapter introduces the scientific context and important features of Cosmic Rays. It also introduces the basic concepts of neutrino interactions, neutrino oscillations and sources.

2.1 Cosmic Rays

Cosmic Rays (CRs) were studied and discovered in 1912 by the physicist Victor Hess³, winner of the Nobel Prize in Physics in 1936. Hess used an aerostatic globe and electroscopes to show while ascending from the Earth's surface, as a counting experiment, ionization increases proportionally with the altitude. He concluded that any radiation must be coming from outside the Earth. About 10,000 CRs hit every second, each square centimetre of our Earth with charged subatomic particles at very high energies.⁴ CRs are fast-moving particles traveling at nearly the speed of light from space that arrive evenly from all directions of the sky. Depending on their nature, they are deflected continuously and scattered by magnetic fields in the galaxy until any trace is lost of their original motion. Simple protons (hydrogen nuclei) are most of the common identified CRs, other fraction are identical to helium nuclei (i.e., alpha particles) and a small fraction are the nuclei of heavier elements. Some of them are the most energetic of any particles ever observed in nature, and their interactions with matter and fields are the wellspring of a significant part of the diffuse γ (gamma)-ray, X-ray, and radio emissions that are observed.⁵

Figure 2.1 shows a global view of the large spectrum of CRs with the distribution of energy. Their energy spectrum reaches several orders of magnitude and follows, to a very good approximation, a power law. The differential flux can be written as⁴

$$\frac{dN}{dE} \propto E^{-\gamma} \quad (2.1)$$

with γ being called the spectral index. The range of energy in the transition ranges are known as the "knee" and the "ankle". Energy close to $\sim 10^{15} eV$ represent the "knee" of the spectrum and corresponds to a change of spectral

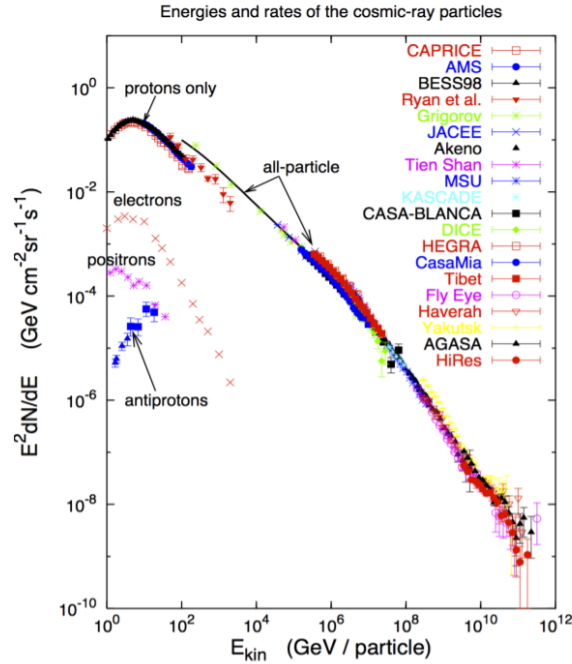


Figure 2.1: **Cosmic Ray energy spectrum:** Global view of the cosmic ray range of energy spectrum. All data are recollected for several experiments as indicated.⁴

index from $\gamma \approx 2.7$, but a second "knee" is seen close to $\sim 10^{17} eV$. The energy spectra may be characteristic of some types of certain acceleration mechanisms.⁴ The "ankle" is around $\sim 10^{18} eV$ energy, it suggest the existence of particles of extragalactic origin. The energy spectrum below $10^{18} eV$ is considered as very-High Energy (VHE) cosmic rays. The range between $10^{18} eV$ to $10^{19} eV$ is known as UHE cosmic rays, and after that range of the ankle is called the Extrem Energy (EE). The CR spectral index γ values represent important transitions in the slope. CRs after a century constitute one of the most energetic forms of extraterrestrial radiation traveling to the Earth at relativistic speeds from the deep space. Questions about how the particles accelerate to reach such high energies? and where do they come from?" are not still clearly replied.

Technically, CRs are classified in primary and secondary particles. Primary particles are stable charged particles that have been accelerated to enormous energies by astrophysical sources somewhere in our Universe. When primary CRs interact with the Earth's atmosphere, create Air Shower (AS) or Extensive Air Shower (EAS) producing cascades of secondary particles. In the interaction of secondary CRs muons and neutrinos are produced as a result of the decay of charged mesons (quark + antiquark pair). Each EAS produces mainly two light components that are fluorescence and Cherenkov light.⁶ We can infer about the energy of CRs from the site of acceleration, Galactic Cosmic Rays (GCRs) and Extragalactic Cosmic Rays (ECRs), for instance, potential sources which could give the observed flux of

high energy cosmic rays includes Active Galactic Nuclei (AGNs), Gamma Ray Bursts (GRBs), Supernova Remnants (SNRs), Pulsars, interacting galaxies, Blazars.⁷

The importance of the information that neutrinos and gravitational waves carry on from the inner regions of astrophysical sources is essential to understand our Universe better. The features of neutrino interactions make high energy cosmic neutrinos the ideal candidate for finding the position of CRs sources, pointing to the correct direction.

2.2 Neutrinos

Neutrinos are chargeless leptons weakly interacting, so, do not deflect by magnetic fields or absorbed by matter, having a small cross-section when interacting with other particles. Wolfgang Pauli in 1930, postulated about the (electron) neutrino in his famous letter to Lise Meitner et al.⁸, in which explain the result of the continuous spectrum of electrons from radioactive beta decays. Pauli proposed that in the final state of the decay, add a third, uncharged and massless particle to maintain energy, and momentum conservation.

$$n \rightarrow p + e^{-} + \bar{\nu}_e \quad (2.2)$$

It took 26 years to prove the existence of the (electron) neutrino by Reines and Cowan⁹ in 1956 in a nuclear reactor experiment. After that, two more neutrino flavors became discovered, namely the muon¹⁰ and tau¹¹ neutrino. The particles are grouped into three lepton generations, corresponding to the three generations of quarks as shown in Figure 2.2 completing the table of the "Standard Model (SM) of Elementary Particles". For each of these fermions (leptons and quarks), there exists an antiparticle partner. Each neutrino is associated with their charged leptons, e , μ and τ . The neutrinos are assumed to be massless and only coupling to other particles via the weak interaction by Standard Model (SM) exchanging W^{\pm} and Z bosons, charged and neutral current interactions respectively. However, the observation of neutrino oscillations¹² implies that neutrinos have non-zero mass, and it implies physics beyond the SM (BSM). This behaviour is explained by the oscillations of neutrinos between different flavor (types) eigenstates.

2.3 Neutrino interactions

Neutrinos are weakly interacting, due to their low cross-section, and chargeless, can not be directly detected. The indirect detection of neutrinos is possible when a neutrino is interacting with a nucleon of the surrounding matter. It produces a charged particle (lepton) inducing detectable signal in the medium (e.g Cherenkov light). The cross-section increases with energy, as shown in Figure 2.3, so large volume detectors like KM3NeT are needed.

The neutrino detection is possible by the interaction exchange of W^{\pm} and Z^0 , categorized into two types interactions: Charged Current (CC) and Neutral Current (NC). In NC interactions represented in Figure 2.4(a), the neutrino remains as the same neutrino flavor; on the other hand, Figure 2.4(b-c-d) in the CC interaction, the neutrino transforms

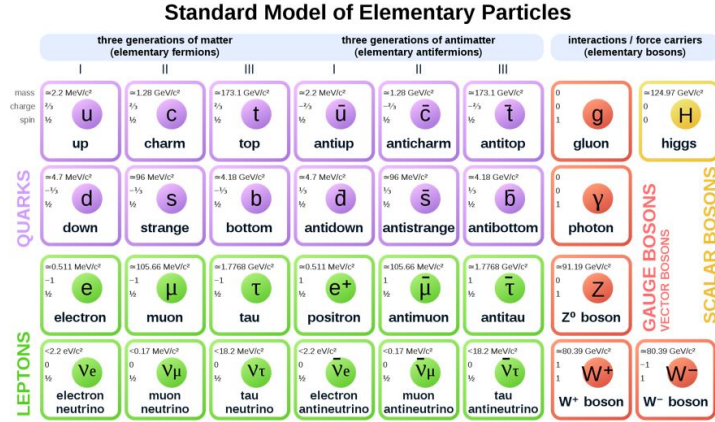


Figure 2.2: **Standard Model of Elementary Particle.** Summary and classification of all elementary particles forming the building blocks of matter.

into a charged lepton. As mentioned before, charged leptons refer to e , μ and τ . Neutrino detectors are usually buried into sea-water, ice, or rock because background suppression requirement. KM3NeT aims to study neutrino interactions with the sea-water where secondary charged particles are created, looking at the event signature that is produced by each neutrino flavor. In the case of electron neutrino (ν_e), it creates hadronic shower and electromagnetic cascade (electron) as a signature. For muon neutrino (ν_μ) it creates a hadronic shower, and a muon, which depends on the energy can travel at relatively long distance. The tau neutrino (ν_τ) creates the hypothetical "double bang" interaction (not seen yet), creates two hadronic showers and/or electron showers, and a tau particle. Tracks of muons give the best angular resolution and the best pointing accuracy, it is the golden channel for neutrino telescopes as KM3NeT.

2.4 Neutrino oscillation

For a long time, the neutrino was thought to be massless. It is due that neutrino has features in which the flavor eigenstates are not equal to mass eigenstates. Instead of that, the three flavor eigenstates are a mixture of the three mass eigenstates with unequal masses. This behaviour is known as neutrino oscillation, which has been able to explain the reduction in solar electron neutrino and the missing atmospheric muon neutrino flux. The evidence of oscillations results was presented by of SNO (Sudbury Neutrino Observatory) and Super-Kamiokande, which in 2015 were awarded of Nobel Prize in Physics.¹⁴ Neutrino oscillation refers to periodic changes of the probability of a neutrino produced in an eigenstate α to be detected in another eigenstate β , where $\alpha \neq \beta$, when travelling over macroscopic distance.

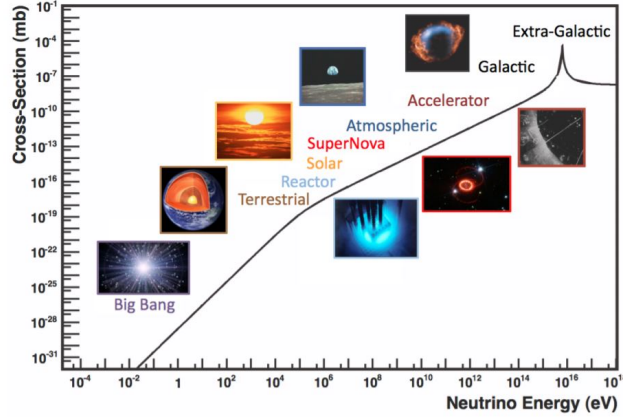


Figure 2.3: **Neutrino interaction cross section as a function of energy.** Neutrino interaction cross section scales as a function of energy, the range of energy given some sources of neutrinos are also illustrated.¹³

2.4.1 Mixing of neutrino eigenstates and oscillation parameters

Flavor eigenstates usually denoted as $|\mu_\alpha\rangle$ ($\alpha = e, \mu, \tau$) are eigenstates of the weak interaction. The three mass eigenstates denoted as $\langle\mu_k|$ ($k = 1, 2, 3$) describe the free particle evolution, eigenstates of the corresponding Hamiltonian. These eigenstates have to be considered when describing the propagation of neutrinos in vacuum. In a practical way, transformations between neutrino flavor and mass eigenstates can be expressed as:

$$|\nu_k\rangle = \sum_{\alpha=1,2,3} U_{\alpha k} |\nu_\alpha\rangle \quad (2.3)$$

$$|\nu_\alpha\rangle = \sum_{k=1,2,3} U_{\alpha k}^* |\nu_k\rangle \quad (2.4)$$

where $U_{\alpha k}$ are the elements of the unitary neutrino mixing matrix U . This neutrino mixing matrix is often called PMNS (Pontecorvo, Maki, Nakagawa, and Sakata) matrix.^{15 16} The matrix U can be parameterised by three mixing angles θ_{ij} , and one complex phase δ that is related to possible CP violation:¹⁷

$$U = \begin{pmatrix} 1 & 0 & 0 \\ 0 & c_{23} & s_{23} \\ 0 & -s_{23} & c_{23} \end{pmatrix} \begin{pmatrix} c_{13} & 0 & e^{i\delta} \\ 0 & 1 & 0 \\ -e^{i\delta} s_{13} & 0 & c_{13} \end{pmatrix} \begin{pmatrix} c_{12} & s_{12} & 0 \\ -s_{12} & c_{12} & 0 \\ 0 & 0 & 1 \end{pmatrix} \quad (2.5)$$

where $c_{ij} \equiv \cos\theta_{ij}$ and $s_{ij} \equiv \sin\theta_{ij}$. The first matrix can be studied with atmospheric neutrinos and LBL (Long-Base-Line) accelerators, the second one with SBL (Short-Base-Line) reactors and the third one with solar neutrinos and LBL reactors. KM3NeT-ORCA is expected to give important insights about neutrino oscillations parameters and δ_{CP} with very competitive limits.²

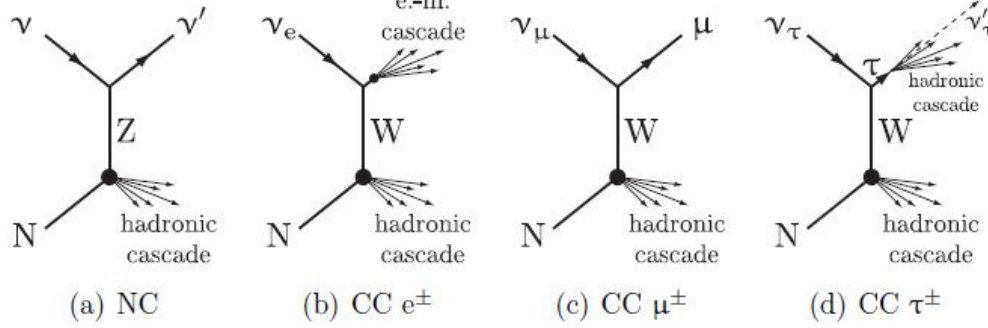


Figure 2.4: **Neutrino interaction channels.** a) Neutral Current that results as hadronic cascade and an invisible outgoing neutrino. b) Charged Current of electron neutrinos that produce an electron and instantaneously an electromagnetic cascade. c) Charged Current Muon neutrino that produces hadronic cascade and a muon and d) Charged Current tau neutrino that produces a hadronic shower and a tau, tau decays fast and produce an additional hadronic or electron cascade.

2.4.2 Neutrino Mass Hierarchy (NMH)

From the three neutrino mass eigenstates, three mass-squared differences can be constructed, but only two of them are independent:

$$\Delta m_{32}^2 + \Delta m_{21}^2 = \Delta m_{31}^2 \quad (2.6)$$

The relative ordering of the three neutrino mass eigenstates has not been resolved yet. To determine the Mass Hierarchy (MH) between the neutrino flavors oscillation probabilities are needed. There are two possible non-equivalent orderings for the mass eigenvalues. The convention is to choose m_1 and m_2 as the mass eigenstate that are close to each other, with $m_1 < m_2$. The third mass eigenstate is separated from the other two, either above or below. The ordering $m_1 < m_2 < m_3$ is customary referred to as Normal Hierarchy (NH) and $m_3 < m_1 < m_2$ as Inverted Hierarchy (IH). Both possible NMH scenarios are illustrated in Figure 2.5. Sensitivity to distinguish between NH \leftrightarrow IH is $\sim 3\sigma$, expected to be reached in three years once KM3NeT is completed (in median sensitivity).²

2.5 Neutrino Sources

This section summarises the most promising sources as candidates of CRs, UHECRs and therefore HE cosmic neutrinos that thought share the same origin. High-energy cosmic neutrinos are uniquely poised to explore them in a strange and otherwise unreachable energy and distance regime. Some of the theoretical scenarios include (some of them tested with data):

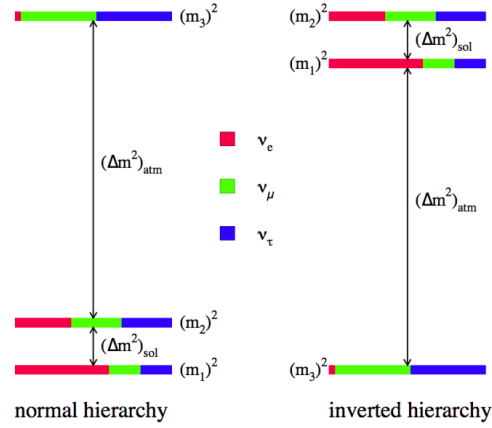


Figure 2.5: **Scheme of NMH.** Each neutrino flavor is represented by a color. Normal and Inverted Hierarchy representations are shown.¹⁸

2.5.1 Extra-galactic origin

Active Galactic Nuclei (AGN). Refers to galaxies with a supermassive black hole in their centre and an accretion disc surrounding it.¹⁹ The magnetic field is created to keep an angular momentum in the ejected direction perpendicular to the Galactic plane in relativistic jets. High-energy neutrinos emission is expected along with these jets. High-energy gamma rays are also emitted from AGNs along with their jets. There are different names to AGNs depending on the direction of the jets and also the direction of the observer :

- Seyfert Galaxy: the observation axis is between the rotational axis (direction of the relativistic jets) of the AGNs and the Galaxy plane.
- Blazar: AGNs is a blazar when the rotational axis is pointing to the observer direction.
- Radio Galaxy: the observer axis balance with the Galactic plane.

Gamma-Ray Bursts (GRBs). They are transient phenomena with a lifetime of up to several hundred seconds, emitting a gamma-ray flux that outshines all other gamma-ray sources. They are randomly distributed on the sky, so current models assume them to be extragalactic objects. Currently, GRBs are associated either with the core collapse of a very massive star leading to the formation of a black hole (so-called long-soft GRBs) or with the merger of binary systems consisting of two neutron stars or a neutron star and a black hole (short-hard GRBs). In both cases, matter is ejected from the object in ultra-relativistic jets.²⁰

Starburst Galaxies. They are Galaxies with a high rate of star formations and have been suggested as neutrinos emissors. Observations of synchrotron radiation at radio wavelengths and TeV rays from their dense core regions imply the existence of relativistic electrons. Assuming that protons are accelerated along with these electrons,

the dense core regions with high matter densities can act as proton beam dumps. Neutrinos from the resulting proton-proton interactions could potentially be detected by neutrino telescopes like KM3NeT and IceCube.²¹

2.5.2 Galactic origin

Supernova Remnants (SNRs). One possible source of Galactic cosmic rays and therefore presumably of neutrinos are the remnants of supernovae, as the material emitted from the initial explosion that encounters the interstellar medium and builds a shock front. The measured gamma-ray spectra from SNRs can be used to calculate approximate neutrino rates from these objects, making detection of neutrinos from these sources possible with cubic kilometers detectors as KM3NeT final layout.

Pulsar Wind Nebula (PWNe). Whenever the axis of a magnetic field of neutron stars points into our direction, we possibly observe the object as a pulsar. "Pulsar Wind Nebulae" refer to particles accelerated to relativistic energies, and they can subsequently react with the surrounding matter, some of the brightest sources in TeV gamma rays. Though the gamma acceleration process is usually assumed to be leptonic, it has been suggested that there may be hadronic part in the pulsar wind, which makes the production of neutrinos possible.

Microquasars. They are another candidate for neutrino production. They are binary systems consisting of a neutron star or black hole of approximately a solar mass and single star. The compact object accretes mass from the star and produces a relativistic jet perpendicular to the accretion disc. It has been suggested that these objects may emit high energy neutrinos. It has been argued that rays emitted from microquasars may be heavily absorbed inside the source. Neutrino fluxes for these sources could thus be much higher than predicted from their TeV- γ ray spectra.

2.5.3 Other neutrino sources

There is a multitude of other suggested neutrino sources, among them, various dark matter models and more exotic 'top-down' models suggesting that neutrinos may be produced by super-massive relic particles from the Big Bang. There are too many questions with no answers about our universe yet, and for that reason, experimental particles physics is trying to discover the ways how to solve the problem. Large-scale underwater neutrino telescopes are called to solve lots of answers still unsolved. In the next chapter, KM3NeT undersea neutrino telescope will be described.

Chapter 3

The KM3NeT Neutrino Telescope

In this chapter KM3NeT will be explained. Its detectors network are suited for Cherenkov radiation detection as a result of neutrino interaction with matter. KM3NeT will be able to study neutrino interactions at a GeV-PeV range with the ARCA and ORCA layouts, sharing the same technology but different scaling, addressed to reach the scientific goals through different fluxes and energy ranges. As mentioned, KM3NeT physics goals are based on the discovery and subsequent observation of high-energy neutrinos sources in the Universe and the determination of the NMH. The successful deployment and operation of the ANTARES neutrino telescope have demonstrated the feasibility of performing neutrino studies with large volume detectors in the deep sea.²² The optical detection of neutrinos is based on the reconstruction of Cherenkov light events produced by relativistic particles emerging from a neutrino interaction.

In order to understand KM3NeT functioning, Cherenkov radiation, detector design and other technical aspects are explained below.

3.1 Cherenkov radiation and propagation

Charged particles travelling through a transparent medium with a velocity greater than the group velocity of light in that medium induce Cherenkov light²³. This is the effect that allows neutrino telescopes to reconstruct muon track directions from position, timing and amplitude of hits of light in the optical sensors. Cherenkov light is emitted on a cone with the emitting particle on its tip and with a characteristic opening angle θ_C depending on the particle's speed ($\beta = \frac{v}{c}$) and the refractive index (n) of the medium:

$$\cos \theta_C = \frac{1}{\beta n} \quad (3.1)$$

For seawater with $n \sim 1.35$ ²⁴ and for highly relativistic particles (i.e. $\beta \sim 1$) the Cherenkov angle approaches

$\theta_C = 42^\circ$ and becomes independent of the particle energy. When neglecting changes in refractive index, the Cherenkov radiation intensity is proportional to the emitted photon frequency. As water is only transparent in a narrow band within the visible spectrum, most of the Cherenkov light is visible in the ultraviolet and visible range. The number of photons emitted from a charged particle per path length can be written as

$$\frac{d^2N}{dx d\lambda} = \frac{2\pi\alpha}{\lambda^2} \left(1 - \frac{1}{n^2\beta^2}\right) \quad (3.2)$$

where λ is the wavelength of the Cherenkov photon and α is the fine-structure constant. The relevant wavelength range for water-based neutrino telescopes is 300-600 nm, the number of photons per track length then should be close to

$$\frac{dN}{dx} = 3.4 \times 10^4 m^{-1} \quad (3.3)$$

As the arrival times of photons in the detector is crucial in the reconstruction of tracks, the speed of light in the specific medium needs to be known as well as the optical properties of the medium. The relative speed is the group velocity of light, which is related to the medium refractive index n by:

$$v_g = \frac{c}{n} + \lambda \frac{c}{n^2} \frac{dn}{d\lambda} \quad (3.4)$$

where, n_g is the group refractive index is defined, the $v_g = \frac{c}{n_g}$. Now equation 3.4 is rewritten

$$n_g = \frac{n}{1 + \frac{\lambda}{n} \frac{dn}{d\lambda}} \quad (3.5)$$

Refractive index in sea water have to be measured, dependent on temperature, salinity and water pressure at a certain point. At 470 nm, the values of $n \approx 1.35$ and $n_g \equiv 1.42$.²⁴

The optical properties of the surrounding medium influences the Cherenkov light detected by a neutrino. Light propagation through deep-sea water is affected by two effects: absorption (photon-disappearance) and scattering (change of direction of photons), combined into the transmission length of light:²⁵

$$\frac{1}{\lambda_{tr}} = \frac{1}{\lambda_{abs}} + \frac{1}{\lambda_{sca}} \quad (3.6)$$

Low absorption lengths needs a specific density of the detector instrumentation, as particles passing through sparsely instrumented detectors can be lost because all their Cherenkov light is absorbed before it even reaches the sensor. On the other hand, scattering lengths commonly describes the scattering properties of water λ_{sca} and a scattering angle distribution $\beta(\theta)$.²⁶ Scattering processes in which only the direction of the light is changed are dominant, whereas scattering phenomena in which also the photon wavelength changes (e.g. the Raman effect) happen less frequently. Scattering can take place on molecules (Rayleigh scattering) or particulate matter (Mie scattering).²⁷

3.2 Detector Design

This section is booked for technical details and design of KM3NeT. Each part of the detector plays an important role in design and mechanics. As mentioned before, ARCA and ORCA used the same detector technology, but different scaling.

3.2.1 The Digital Optical Module (DOM)

The KM3NeT DOM is a 17" pressure-resistant glass sphere, housing 31 3-inches PMTs and the readout electronics.²⁸ The DOM registers the time of arrival of the Cherenkov photons generated in the seawater by charged particles in neutrino interaction inside or close to the detector. The DOM also measures how much bright the light (amplitude of the pulse) and the geometrical position at the time of arrival of the photon of the sensor. Figure 3.1 shows a KM3NeT DOM ensemble. PMTs as one of the main devices in the DOM is subject of this work, and better explained in the next chapter.



Figure 3.1: **The KM3NeT DOM.** A DOM consists of a glass spherical vessel, 31 PMTs arranged to look in all directions, LED, CLB, PB, associated readout, power supply and communication.

The DOM design consists of a 432 mm diameter borosilicate glass sphere that contains 31 PMTs, power supply, calibration devices, control and communication.²⁹ The glass is separated in two half parts, top and bottom before assembly integration. The PMTs are placed in rings, five rings are of 6 PMTs starting from the top, and in the bottom, the last ring is just for one PMT pointing straight down. The arrange allows looking in all directions for the faint light emitted by particles crossing the detector. The 31 PMTs are installed in a 3D printed shaped support structure. The support structure also holds reflector rings surrounding the PMTs, a pressure gauge and a LED beacon. The reflector rings are designed to improve the detection of light and the sensitive area of the PMT. A transparent gel is used to ensure the optical coupling between the PMTs and the inner surface of the glass spheres. The top hemisphere of the DOM has a perforation for passing two copper wires and optical fiber, in order to provide power, communication and

data sending. Furthermore, several instruments are mounted inside the DOM to measure its position and orientation (compass, tilt-meter, acoustic sensor) and to time-calibrate the DOMs (light emitters based on LEDs). When the two parts of the sphere are assembled, a titanium collar is around the sphere and is used to mount the DOM on a support structure called Detection Unit (DU).

The main electronics boards inside the DOM are the Power Board (PB), the Central Logic Board (CLB), the signal processing boards and the PMT bases.²⁹ Figure 3.2 shows two of the electronic boards used in the DOMs. The PB converts the incoming 12V to the needed voltages via high-efficiency DC/DC converters. The PMT base connected at the rear contains a Cockcroft-Walton which guarantee the required and adjustable High-Voltage (HV). A second custom Application-Specific Integrated Circuit (ASIC) contains a pre-amplifier, comparator and low-voltage differential-signal (LVDS) driver which gives a high signal and turn the PMT pulse into a digital signal, while the pulse is above an adjustable threshold. Besides there are two signal detection boards, in the top and bottom of the DOM, their route the PMT signals to the CLB and provide a connection for the piezo-electric hydrophone. The CLB has a Field-Programmable Gate Array (FPGA) which implements the whole data, data-acquisition, time synchronization and optical Ethernet communication. The CLB is connected to a LED Beacon called "nanobeacon" through the FPGA, and this assures that the beacon trigger rate and voltage can be set from shore. The "nanobeacon" is the main device together with the PMT, for timing calibration of KM3NeT. A multi-wavelength nanobeacon is one of the current discussions of extended use for optical calibration purposes for KM3NeT next phase.

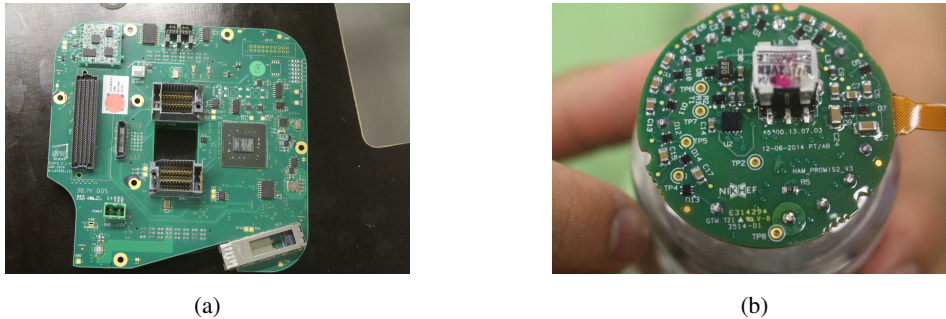


Figure 3.2: **Main electronics boards of the DOM.** a) Central Logic Board (CLB). b) PMT base mounted.

3.2.2 Detection Unit (DU)

A Detection Unit (DU) gathers 18 DOMs connected by a cable and arranged in a vertical line.² There are two 4 mm ropes made by Dyneema,²⁹ working as the mechanical backbone, this is connected to the DOM with the titanium collar. Moreover, a DU contains an anchor, the weight of which keeps the DU connected to the bottom of the seabed. On the top of DU has buoyancy to reduce the horizontal displacement for the case of strong sea currents. Inside the ropes is the Vertical Electro-Optical Cable (VEOC), a pressure-balanced, oil-filled, plastic tube that contains

two copper wires for the power transmission.²⁹ Figure 3.3 shows the DU scheme at the bottom of the sea connections.

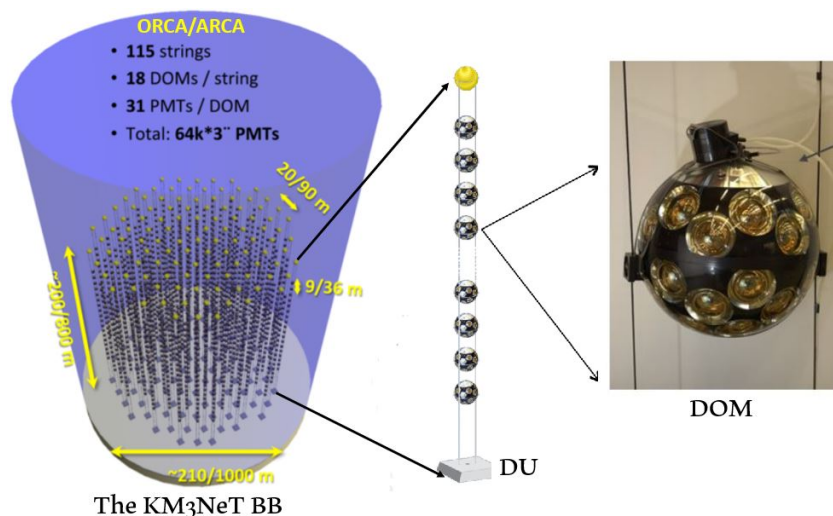


Figure 3.3: **Scheme of 115 Detection Unit (DU) forming a Building Block (BB)**. It is a representation of what is expected to be fully operating at the abyssal sites of KM3NeT once completed. BB describes the complex structure and distances for ORCA/ARCA. A close view of a DU with buoys and anchor dead weight is represented, additionally, it shows how two ropes connect the DOMs.

KM3NeT detectors will consist of blocks or structures of 115 DUs, called Building Blocks, described in the next section.

3.2.3 Building Blocks (BB)

A detector Building Block (BB) consists of an arrangement of 115 DUs. ARCA includes two BBs and ORCA one BB, they use the same detectors and technology but a different scale and separations between the DOM and DU as commented, as a function of their scientific goals. Figure 3.3 shows an illustration of the 115 DU forming a BB.

The instrumented volume of the two ARCA blocks will be about one cubic kilometre. DOMs distance along the string units is about 36 m, and the distance between units is about 90 m. The height of these blocks is about 800 m, and the radius is about 500 meters. On the other hand, in ORCA, the distance between DOMs along the unit is 9 m, and the distance between units is 20 m. This arrangement is almost 250 times smaller than the ARCA detector, with a radius of around 212 meters. Figure 3.4 shows the ARCA and ORCA BBs, in their final layout, in order to compare the size of the both neutrino detectors forming the KM3NeT neutrino observatory.

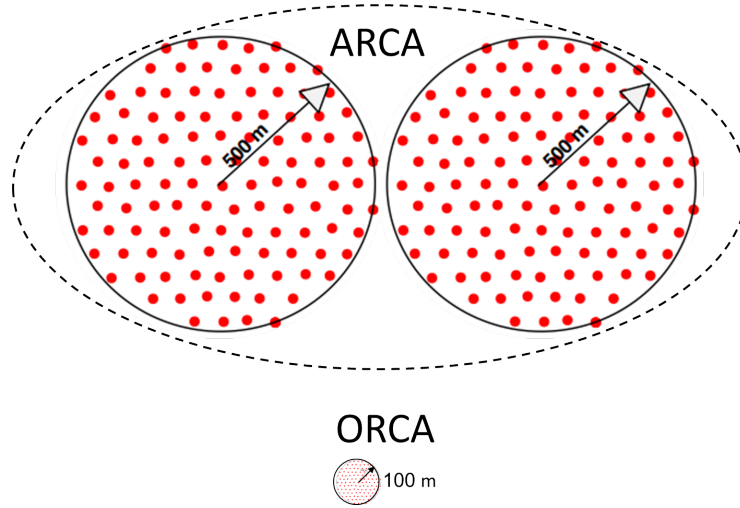


Figure 3.4: **Building Blocks in KM3NeT.** ARCA consist of 2 BBs and ORCA just one. This illustration compares the difference of the scales, function of their scientific goals.

3.3 Background sources

Undersea neutrino telescopes collect Cherenkov light regardless of the source, it is mandatory to distinguish the signal from the background (used for calibration in KM3NeT). The detector has two main sources of background: optical (^{40}K + bioluminescence) and physical (atmospheric muons and neutrinos). Additionally, the counting rate of each PMT is not only high due to light sources, it is about 7KHz, but dominated by background at the site.

3.3.1 The optical background

Decay of ^{40}K . The main contribution of optical background is the hit rate from the ^{40}K decay. In the seawater the salt includes a small amount of the radioactive isotope potassium-40 (^{40}K), which decays through β decay with a ratio of 89,3% ($^{40}\text{K} \rightarrow ^{40}\text{Ca} + \bar{\nu}_e + e^-$) with an energy of 1.31MeV. An electron must have an energy greater than 175 keV to go faster than light in water and produce Cherenkov light. Beta electrons of radioactivity often fulfil this condition. The resulting electrons have an energy of about 1MeV, which is sufficient to produce Cherenkov light. These electrons can emit a constant background signal in the detector. The ^{40}K background is correlated between PMTs on the same DOM while the neutrino signals are correlated between DOMs. There are suspicions that DOM glass also contains a certain amount of ^{40}K , but it is actually an ongoing study, looking to infer about manufacturing process influence and/or production models variation.

Bioluminescence. KM3NeT is in the bottom of the sea, as part of sea environment that contains a large number of

life forms, ranging from microscopic to macroscopic organisms. Several of these organisms emit light in a broad range of wavelengths. Bioluminescent organisms produce background on the detectors. The contribution of the bioluminescence to the signal is called the burst fraction.³⁰ Bioluminescence is subject to a noticeable seasonal variation. The KM3NeT collaboration measures a baseline noise rate in the range of about 7 to 8 kHz with rates of over a MHz during bursts.

3.3.2 The physical background

Atmospheric muons and neutrinos

When CRs interact with the atmosphere it produces a cascade of secondary particles in which muons and neutrinos are produced. The background signal is produced when these high-energy atmospheric muons reach the detector from above, or atmospheric neutrinos induce signal in the detector vicinity. This kind of backgrounds is one of the main reason to build neutrino detectors at deep sites as water, ice or rock. Therefore, neutrino telescopes predominantly look at up-going muons because atmospheric muons can not reach the detector from below (up-going). Despite the irreducible atmospheric muon-neutrino induced background, only identified by the hardness of the energy spectrum.

The complex design of KM3NeT neutrino telescope gives an idea how the experimental particle physics is growing up at big steps, engineers and technicians, forming a multi-disciplinary team in order to know more about neutrino science and technology. Next chapter the details about PMTs, one of the main components of KM3NeT and subject of this thesis is described.

Chapter 4

Photomultiplier Tubes

In this chapter, the main features of a Photomultiplier Tube (PMT) will be presented. KM3NeT uses PMTs as its underwater light sensors. For this experimental research, the understanding of the behavior and characteristics of PMT are crucial to obtain the expected performance of the DOM, the DU and KM3NeT in a whole.

4.1 Properties of PMTs

PMTs was the first device to detect light at the single-photon level invented more than 80 years ago,³¹ today, PMTs are widely used in many applications including industry, medicine and academic research where high sensitivity light sensors are required³². PMTs are devices that convert the incoming light photons to an output electrical signal. It consists of a photo-cathode, anode and electron multiplication system. When an incident light photon hits the photo-cathode, it produces an electron by the external photoelectric effect. The electron, when it hits the first dynode starts to generate a multiplication of electrons by secondary emission to the next dynode, and this is repeated until arriving at the anode, where the output signal (current) is collected. Each dynode multiplies via Poisson process the amount of electrons. Figure 4.1 shows this process across the main components of the PMT.

PMT models vary in the number of dynodes, the geometry, spectral response range and depending on the application purpose. For the KM3NeT neutrino detector is crucial that some properties like the Gain, that is related of the total amount of electrons that were liberated by the multiplication of secondary emission, reaches $\sim 10^6 - 10^8$, among other specific requirements as commented in brief.

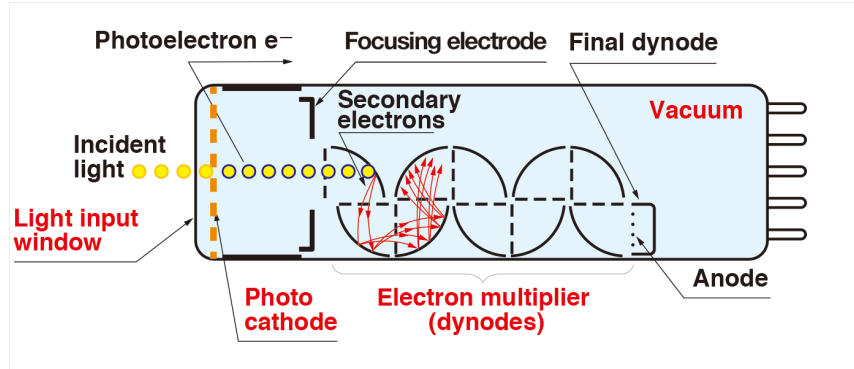


Figure 4.1: **Scheme of the working principle of a PMT.**³² A photon hits the photo-cathode and produces an electron, and the electron is focused to the first dynode, where the electron starts a multiplication process by the emission of secondary electrons, this is repeated until the last dynode to arrive at the anode and readout.

4.2 KM3NeT PMT requirements

PMTs performance and operation in KM3NeT play one of the most important role in neutrino detection. For that reason KM3NeT has specific PMT requirements that are enlisted in Table 4.1:

Parameter	Requirement
Photo-cathode diameter	>72 mm
Nominal Voltage for gain $3 * 10^6$	900/1300V
Quantum Efficiency at 470 nm	> 18%
Quantum Efficiency at 404 nm	> 25%
Peak-to-Valley ratio	> 2.0
Transit Time Spread (FWHM)	< 5 ns
Dark count rate (0.3 spe threshold, at 20° C)	2000 cps max
Prepulses between -60 ns and -10 ns	1.5% max
Delayed pulses between 15 ns and 60 ns	5.5% max
Late afterpulses between 100 ns and 10 μs	15% max

Table 4.1: Main requirements for the 3-inch PMT performance in KM3NeT³³

KM3NeT detector uses the Hamamatsu PMT R12199-02.³³ It is a standard bialkali photocathode with a diameter of 80 mm with ten dynode stages. Figure 4.2 shows the KM3NeT PMT currently under operation. To improve the detection of light inside the DOM, a reflector ring was designed. It is located surrounding each PMT increasing the photocathode area³⁴. The light coming perpendicular to the PMT can be collected by the reflector ring and send to the photocathode avoiding lose of the incoming photon. Figure 4.3 is a scheme of the PMT with the reflector ring

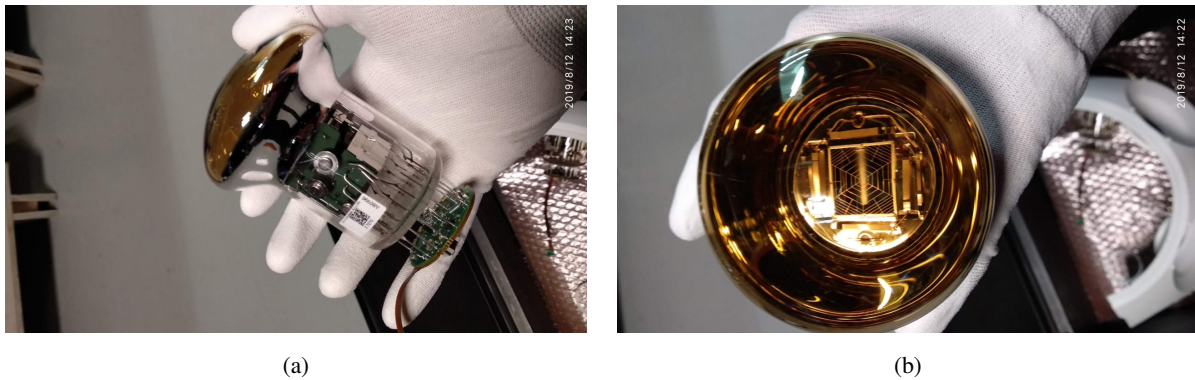


Figure 4.2: **Pictures of PMT used in KM3NeT:** a) Picture of a side view of the PMT with the electronic base. b) Picture of the top view of the PMT. The design of the PMT is crucial to reach KM3NeT scientific challenges

inside the DOM.

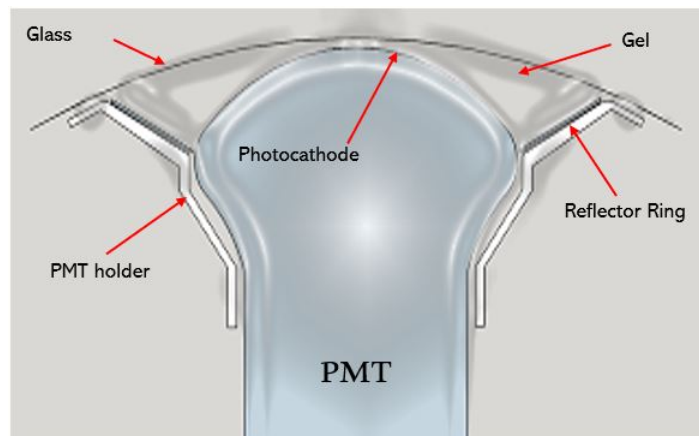


Figure 4.3: **Scheme of the geometry of the reflection ring.** Each PMT inside the DOM is surrounded by an reflector ring that was designed to improve the detection of light, it allows that of light coming perpendicular to the PMT will be collected by reflection sending to the photocathode in order to do not loss the photon.

PMTs are photosensitive devices, the photocathode sensitivity specifies the spectral response of a PMT to light, it can be expressed in terms of Quantum Efficiency (QE) of the photocathode, the Collection Efficiency (CE) of the dynodes, or the Detection Efficiency (DE) that includes both effects. QE is defined as the ratio of the number of photoelectrons emitted from the photocathode to the number of incident photons. CE is associated to the probability that photoelectrons will land on the effective area of the first dynode, area where photoelectrons are multiplied

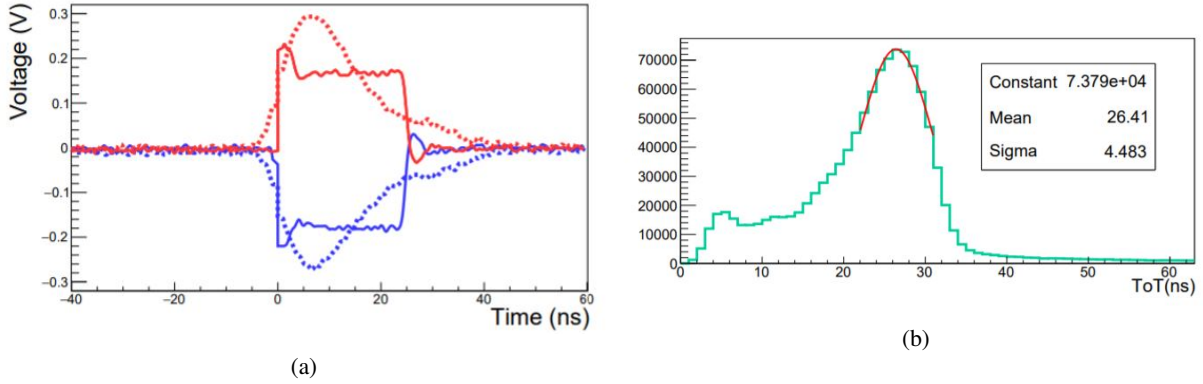


Figure 4.4: **Properties of Hamamatsu R12199-02 PMT.** a) Relation between analogue Voltage vs Time (dashed lines) and ToT (solid lines) signals from the KM3NeT PMT base. b) Typical ToT distribution showing the fit to the peak whose value corresponds to 26.4 ns as required by KM3NeT.³³

effectively at subsequent stages without altering from their favorable trajectories.³² A practical definition related in the work on photon counting mode (KM3NeT PMTs) is the DE or "Counting Efficiency", it is used to express the ratio of the number of counted pulses (output) to the number of incident photons as:

$$DE = \frac{N_d}{N_p}, \quad (4.1)$$

where N_d is the counted value and N_p is the number of incident photons.³² There are many requirements in photodetectors, but this work aims to find a sensitive response obtaining DE (see Section 5.1.3) for a PMT.³⁵

When the electrons arrive at the dynode a pulse signal is generated, that is treated by the electronic PMT base. Figure 4.2 shows the base connected at the bottom of the PMT. The base has been developed to amplify and digitize the signal, and the base contains the electronic to generate the HV required and it is connected to control signals inside the DOM. The base consists of a current amplifier and a settable threshold discriminator. The threshold discriminator converts the analogue signal to a rectangular Time-over-Threshold (ToT) signal as shown in Figure 4.4a.

A Field-Programmable Gate Array (FPGA) is the responsible for digitizing the signal and converting into a hit that contains two variables t and ToT, the time at which the signal has surpassed the threshold, and the total time that signal was above the threshold respectively. As KM3NeT aims for a gain of 3×10^6 in their PMTs, HV tuning in PMTs are required. In order to achieve the desired gain for all PMTs KM3NeT uses the relation between the ToT distribution and the gain. The ToT distribution needs to peak at 26.4 ns to ensure a Gain of $\sim 3 \times 10^6$. Figure 4.4b shows a typical ToT distribution associated to the required gain.

One of the main timing properties of a PMT is the Transit Time Spread (TTS). The TTS is defined at the Full Width

at Half Maximum (FWHM) around the peak of the time distribution. The spread in this peak is a measure for the timing resolution and should be as small as possible to reconstruct efficiently tracks of particles in the detector. Resolution impacts the performance of the detector. Other timing feature is the Transit Time (t_{TT}), which is defined as the time that it takes to detect an analogue signal when a photon hits a PMT. In the photocathode the photons arrive at different positions producing photoelectrons with different trajectories of the path, varying t_{TT} and ToT values, visible in their corresponding distributions. The arrival time (t_a) is also essential, it considers the travel time of the light, the transit time, and the delay in the electronics as a whole effect.

In a PMT the dark rate is the noise pulses that can be measured in the complete darkness (absence of any kind of light). The dark count for a PMT is the spontaneous thermionic emission of electrons from the photocathode. Pulses that result from this process correspond mainly to a single photoelectron. The rate at which these pulses are observed is proportional to the area of the photocathode. KM3NeT PMTs have bialkali photocathodes with the lowest ratio per unit of area.³³ Furthermore, the PMT produces prepulses and afterpulses; there are considered as noise pulses. Prepulses appears from an impact on the first dynode by a direct photo-effect, due to photons that go through the photocathode without interactions. Afterpulses follows the main pulse of a light event, produced by the emission of light from the stages of the multiplier structure, which goes towards the photocathode producing further photoelectrons.³³

Chapter 5

Methodology

In this chapter, a description of the experimental work is explained, a special test bench was built to study the PMTs response in efficiency. The objective of the setup is to measure the Detection Efficiency (DE) of a Photomultiplier Tube (PMT) at different angles and study the angular acceptance response symmetries. The test bench for PMT is based on the Digital Optical Module (DOM) being tested. In an attempt to mimic sea-water conditions, an aquarium filled with tap water was holding the full DOM in a dark environment. Following, the design of the test bench is addressed in this section.

5.1 Experimental setup (test bench)

The analysis of Photomultiplier Tubes (PMTs) data in this study demanded a dedicate setup in a Dark Room at Nikhef laboratory in Amsterdam, one of the main collaborators of KM3NeT. A Dark Room is required for working at the high light-sensitive regime. A Dark Box is also used to suppress as much as possible the noise from external light sources, even, it is covered inside by neoprene located in the Dark Room. Inside the Dark Box, an aquarium was filled with tap water also working as DOM holding, and the water wanted to mimic DOMs on-site operative conditions. In this setup, the DOM can rotate in two different angles by a rotatory table, to avoid floating a weight structure is glued to the support. A picosecond pulsed laser was used, and it was triggered by the nanobeacon of an external Central Logic Board (CLB) responsible for the functioning of the whole DOM. The external CLB and DOM were connected to White Rabbit Switch (WRS) for time synchronization.³⁶ Figure 5.1 shows the setup used in this work.

In Figure 5.2 the Dark Box is open. It contains an aquarium and a pulsed laser collimator. The aquarium used in this experiment was made of glass with a thickness of 7 mm, it has a length and a width of 67 cm and a height of 72 cm respectively. The pulsed laser collimator is in front of the aquarium on a rail that moves in z and x direction. The DOM is connected as in the Detection Unit (DU) but with the support that allows a certain range of rotation in the vertical

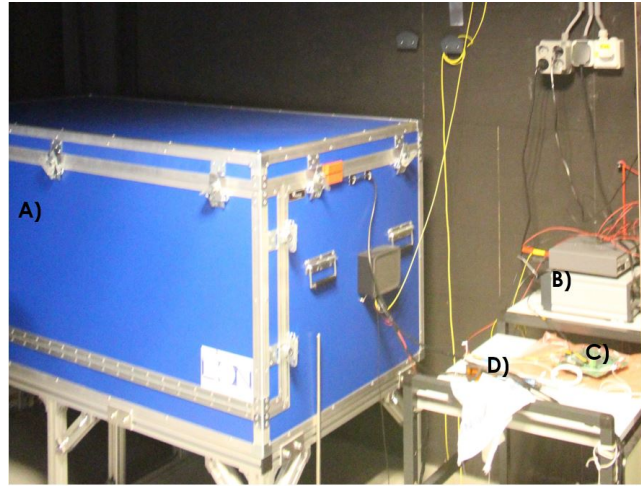


Figure 5.1: **Setup for light detection efficiency studies.** A) Dark box of blue color on the left, it is containing the aquarium with a DOM inside and the collimator. B) It is the pulse generator and the control of electronics of the DOM. C) It is an external CLB used for calibration and triggering the laser D) is the laser driver.

plane. In the horizontal plane rotation, the table has markers of the degrees that allows knowing the rotation in degrees precision. The design of the setup ensures that light can enter through the glass and hits the PMT. The advantage of the possibility of a movable DOM and laser is just the study for different positions of the arrival of light on collection directions. Figure 5.3 shows the possibilities of movable set up in order to obtain different angles of incidence.

5.1.1 Laser setup

As commented before, a laser light source is used in the experimental setup with $\lambda = 401.4$ nm, peak power ~ 530 mW, pulse width of 55 ps and average power of $0.3 \mu\text{W}$. As Figure 5.1 shows the B) pulse generator and D) laser driver, both are outside of the Dark Box, only the light collimator is inside the box. The light of the laser is passing through the optical fiber that is connecting the outside laser driver with the collimator inside. The collimator is on rails that allow move in x and z direction, and always is pointing perpendicular to the glass aquarium. The importance of the laser setup is that it allows us to know when the pulses were sent, possible with an external CLB setting up triggering options. The laser is a picosecond pulsed diode laser with driver produced by ALPHALAS.³⁷

The laser was connected in the external CLB instead of the LED Beacon used for calibrations. The White Rabbit (WR) Software and Hardware is used for triggering the laser using the FPGA of the CLB. The trigger configurations are set by the external CLB connected by Ethernet to the computer. The triggering for the laser signal supposed a pulse period = 24×10^3 ns and the pulse count = 2500 directly sent to the CLB. The pulse count is the number of triggered pulses in a timeslice (collection array of hits in the same time window) of 100 ms. With these settings,

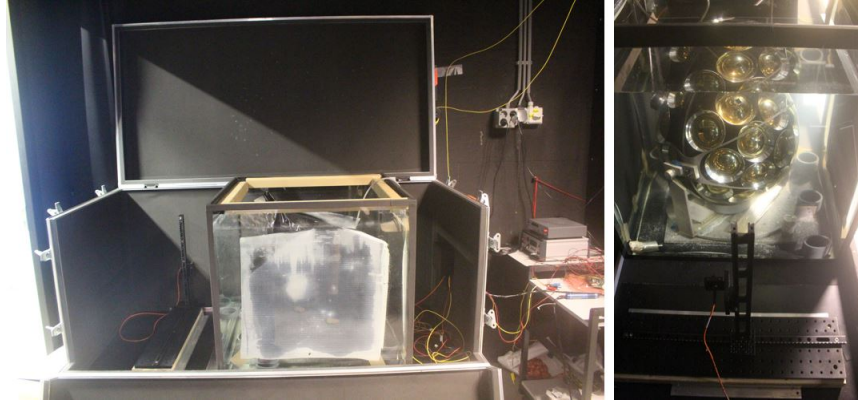


Figure 5.2: **Dark Box.** Left: the dark box used for the experiment. It can be open from one side and the top. The aquarium and the laser collimator are inside. Right: the DOM inside the aquarium. DOM is in rotatory support. The support avoids DOM floating using weights. In front of the DOM is the pulsed collimator laser in a rail that moves in x and z directions

the first $2500 \times 24 \times 10^3$ ns = 60 ms of every timeslice are filled with pulses. The 40 ms remaining of the timeslice was not filled with pulses but was used as a reference to determine the number of background hits. Additionally, Figure 5.4 shows how the DOM and the external CLB are connected to the optical box for signal attenuation, in turn, connected to WRS for time synchronization. The advantage of using WR was the possibility of know when the laser was triggered and when the pulses are expected at absolute calibration.

5.1.2 PMT calibration

An accurate calibration of KM3NeT requires to obtain the same response from the PMTs for a given signal. Although they are made in the same way, but not exactly alike. In KM3NeT, the PMT is calibrated to a Gain of 3×10^6 which corresponds a ToT distribution peak around of 26.4 ns for a single photon. The laser was set for an intensity in which 0.1 of the triggered pulses were detected as single photons. PMTs have a background count rate frequency of 2-5 kHz (dark rate) misconfusing hits coming from the laser, however, background hits are isolated from hits coming from the laser using time correlations. Laser hits are sent with a fixed frequency, while the dark rate hits are uncorrelated in time. For that reason, the use of WR protocol is important to control the pulses sent and arrived with a time offset at the DOM. A small time window of 20 ns is selected in which the pulse is arriving at the DOM.

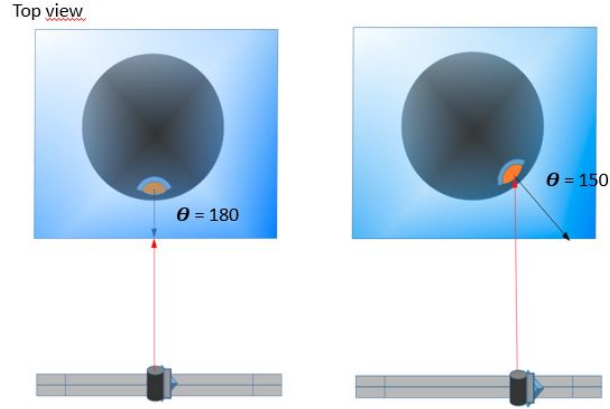


Figure 5.3: **Scheme of the top view of the movable DOM and laser setup.** It is a scheme of the available choices for study at several angles the light detection efficiency. Left the PMT in front of the laser at $\theta = 180$. Right after moving the laser and rotate the DOM by 30° .

5.1.3 Data acquisition

In a the timeslice of 100 ms, the hits are counted in 20 ns time windows around the peak pulse. The arrival time for every photon is known. Furthermore, the laser was set on intensity in which 0.1 of the triggered pulses when hitting the PMT at the center as commented before. When considering a background hit frequency of 5kHz, a number of an average of background hits in this 20 ns time windows are produced by the contamination fraction. This fraction is equal to $5000 \text{ hits/s} \times 20 \times 10^{-9} \text{ s} = 0.0001$. When the laser was not triggered, the background hits are calculated for each measurement by counting the hits of the timeslices. Eventually, the Detection Efficiency (DE) as defined in equation 4.1 can be writing as:

$$DE = \frac{N_{hits} - N_{bg}}{N_{pulses}} \equiv \frac{N_d}{N_p} \quad (5.1)$$

where N_{hits} are the number of hits counted in the 20 ns time windows, N_{bg} the expected number of background hits in these windows and N_{pulses} the number of laser pulses sent in the whole timeslice. In order to make an extensive analysis of detection, some considerations are needed. The laser intensity affects the number of detected hits, and for that reason, it needed to be constant during all the process of experimental sessions. In the same way, the pulse count per timeslice requires to be constant.

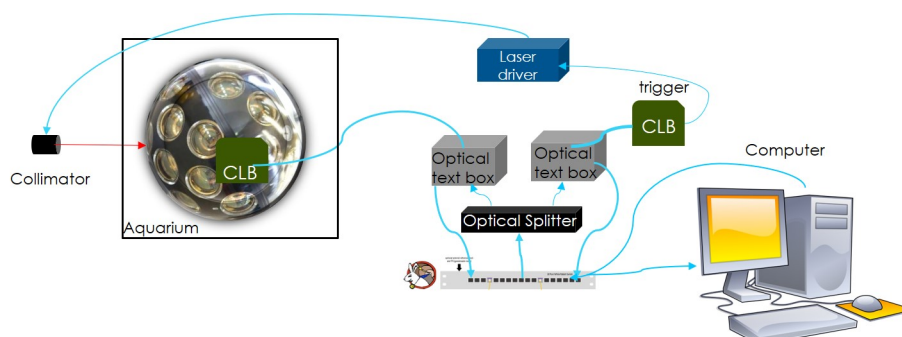


Figure 5.4: **Scheme of the laser setup.** The use of White Rabbit Switch (WRS) guarantees absolute synchronization of time, which the DOM and the external CLB are connected through. This diagram shows the laser driver connected to the external CLB to control laser trigger.

5.2 Data taking routines

In this section, the data collected in the experimental setup is described in detail. All measurements were carried out by using the setup described in section 5.1. In this work, using the same methodology, two different PMTs were tested: one looking to compare the DE at several angles of light incidence and another, selected for finding a symmetry response on light detection in the DOM.

5.2.1 Angular dependence on detection efficiency

Light detection in PMTs is primordial for the objectives of KM3NeT collaboration. In order to study the angular dependence in the detector, several tests were performed. By using an old DOM that was previously considered broken but afterwards repaired, the angular dependence on light DE is studied. The DOM was placed in a rotatory support and put carefully inside the aquarium. Tap water was used to fill the aquarium with the help of a water bomb. The PMT closed to the titanium collar, as shown in Figure 5.5 was selected to start the data taking routine. This PMT was used for several measurements. The titanium collar was not an obstruction to move on with the scheduled routines.

As Figure 5.5 shows, the PMT selected is in front of the collimator. The position of the PMT allowed that the angle between the laser and optical vector was 180° as represented in the diagram of Figure 5.3. The collimator on the rails was moved in four diagonals manually over the PMT and the reflector ring. The separation points size were between 2 and 5 mm, and the spot size is ~ 0.6 mm. Figure 5.6 represents how these diagonals were considered. The PMT and reflector ring were thus consequently analyzed.

Each data point consist of a 60 seconds measurement and during that time the number of hits from the laser were counted, and the light DE was estimated, also the arrival time of photons, and ToT distributions were stored. The efficiencies were linearly interpolated and integrated over the scanned surface. The same methodology was re-



Figure 5.5: **PMT mounting frame.** Left: The PMT close to the titanium collar is marked with a red point for reference. The collimator is on the rails in front of the PMT. Right: Close view of the titanium collar and vertical support.

peated for the same PMT at several angles of incidence. The rotatory frame allowed the variation in angles at $\theta = [180^\circ, 150^\circ, 120^\circ \text{ and } 90^\circ]$ as shown in Figure 5.7.

In the case of the last angle (90°), the four diagonals was not possible due to the position of the laser respect to the PMT. In that special case, a rectangular scan was performed, and the separation between points was bigger. Finally, with the four efficiency scanning plots, the relative angular acceptance was estimated by plotting the integrated efficiencies as a function of $\cos(\theta)$. The function was normalized and compared with the latest OMGsim v2.0 simulations of KM3NeT.²

5.2.2 Symmetry response to light detection

Before the PMTs are located in the DOM to be assembled, they are previously tested looking to obtain the light source response in all directions (as the Cherenkov light by relativistic leptons on-site in the detector). The interest of this work is to study which is the symmetry response of the DOM, to take considerations for simulations and integration in the KM3NeT lines.

The methodology was the same as in section 5.2.1 for angular dependence analysis. The only difference is that other PMT in the DOM was selected for testing. In this case, the goal was to observe symmetry patterns on the detection of light at opposite angles. The angles used were $\theta = [210^\circ, 180^\circ \text{ and } 150^\circ]$. The scheme of the angles for taking data taking routines is presented in Figure 5.8.

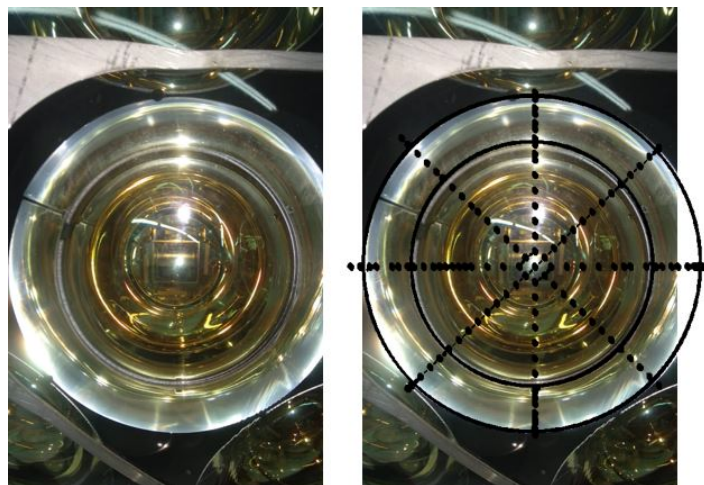


Figure 5.6: **Data points scanning.** Left: the PMT selected closed to the titanium collar. Right: the representation of the 4 diagonals, where each black dots are measurement data. The picture was made through the glass and water.

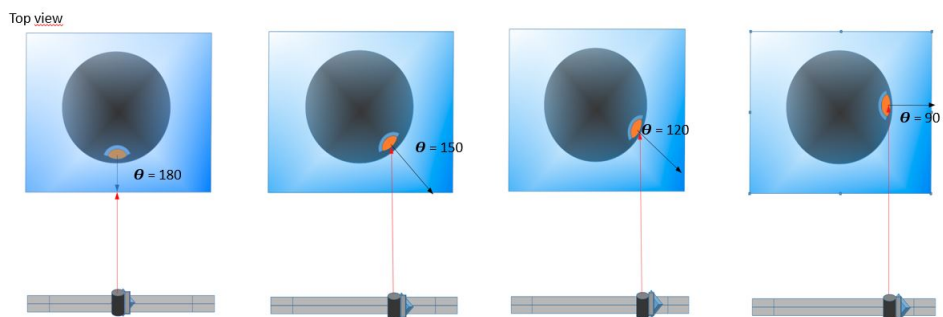


Figure 5.7: **Light source(laser)-light sensor(PMT) orientations for angular dependence studies.** Measurements were taken in four different position of the DOM for the same PMT as figure suggests for scanning DE.

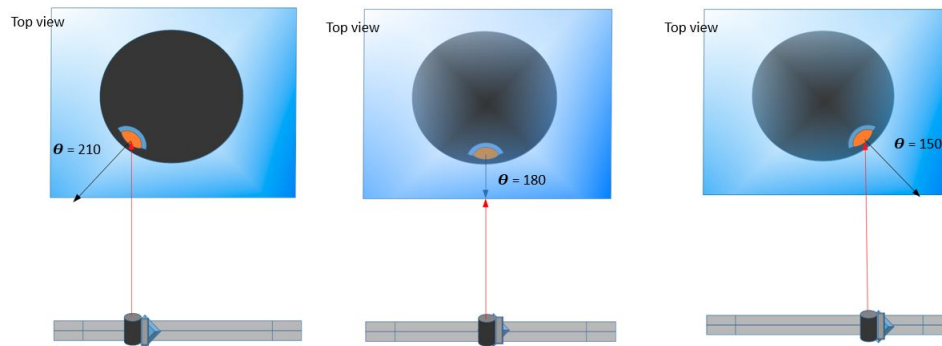


Figure 5.8: **Light source (laser)-light sensor (PMT) orientations for symmetry response studies.** Measurements were taken at 3 different position of the DOM for the same PMT. Mostly the same points were taking at the opposite angles to observe variations in PMT response.

Chapter 6

Results and Discussion

This chapter presents the results and discussion of the two measurements sets for angular dependence and symmetry response studies on light Detection Efficiency (DE) (or simply efficiency hereafter), based on Photomultiplier Tube (PMT) scanning plots of efficiency. Additionally, for the symmetry response, comparisons of ToT distributions and arrival time of photons complement the angular dependence studies. At the end, some remarks on data sets, availability, reproducibility and statistics constraints are presented.

6.1 PMT scanning: angular dependence on light detection efficiency

The results obtained in this work are the continuity of a previous study performed at Nikhef (T. van Eeden), with the help of a dedicated setup (test bench), where eight months were spent on making it successfully functional. The analysis presented in this work was based on scanning different PMTs in the same DOM as explained in Section 5.2.1. Following, each scanning plot at different angles between laser-PMT, referred as "heat maps" will be described and discussed in this section.

6.1.1 PMT scanning: 180° laser-PMT

In this setup, the PMT is in front of the collimator, making an angle of $\theta = 180^\circ$. In this orientation, see Figure 6.1, the efficiency of each 60 s measurements of the four scanned diagonals was stored and a scanning heat map was constructed. In order to obtain a more detailed heat map, more data points are needed. Figure 6.2 shows the result of the efficiency heat maps as first trial on the same PMT. Visually, the plot on the right is more detailed and the plot on the left had less point of measurements. The definition of the heat maps thus depends on the number of data point measurements. An important remark about the difference on the scales must be noticed due to restrictions on the reproducibility of plots because incident reported in Section 6.6. Nevertheless, preliminary conclusions are

extracted carefully taking into account this remark.



Figure 6.1: **Location of the DOM at 180°** . Left: picture of the whole DOM inside the aquarium. Right: view from the line of sight of the laser. The angle between the laser and the optical axis is 180° .

Figure 6.3 summarizes the result of the scan at $\theta = 180^\circ$ for the largest amount of data point measurements, where the DE is quantified in the scale color at right: blue color represent less efficiency, yellow high efficiency. In order to obtain a full heat map the data measurement points were linearly interpolated. The heat map has not a circular shape, it is octagonal due to the four diagonals, and the values of the data points were interpolated. Red and blue lines represent the location of the first and second dynode in the PMT respectively.

As seen in Figure 6.3, several efficiencies zones are non-uniformly distributed. This result can be related, in principle, to the fact of an asymmetric photocathode and dynode configuration. The PMT surface might not be uniform enough. The DE can vary depending on the photon incidence angle and position on the photocathode of the PMT. The uniformity defined by Hamamatsu (PMT suppliers) is described as the variation in the output signal amplitude with respect to the photocathode position.³² As shown in Figure 6.4, Hamamatsu scanned the photocathode area with a laser spot diameter of 1mm at two wavelengths of 400 and 800 nm. The result is that their PMT output varies over the photocathode surface and in general the electron Collection Efficiency (CE) between dynodes may degrade and adversely affect uniformity, thus the DE. This observation might be supported with the heat maps showed above.

Hamamatsu results on the y-axis projection for 400 nm has stronger variations, and it shows around 20 mm how it impacts decreasing the relative output. Figure 6.5 shows the projection for other PMT at 180° , this projection is like the y-axis through the dynodes. A relevant section in the projection is between $[-225, -245]$ mm where the dynodes are referenced with two colored lines, in this range a decrease in the efficiency appears also as Hamamatsu reported in their measurements and setup. Figure 6.5 shows a schematic projection where the PMT region (red dashed lines) is distinguished from the reflector ring and the changes in efficiency along the scanning are also notable. This plot helps to understand how the behaviour of the PMT is, and for that reason a comparison is performed. This

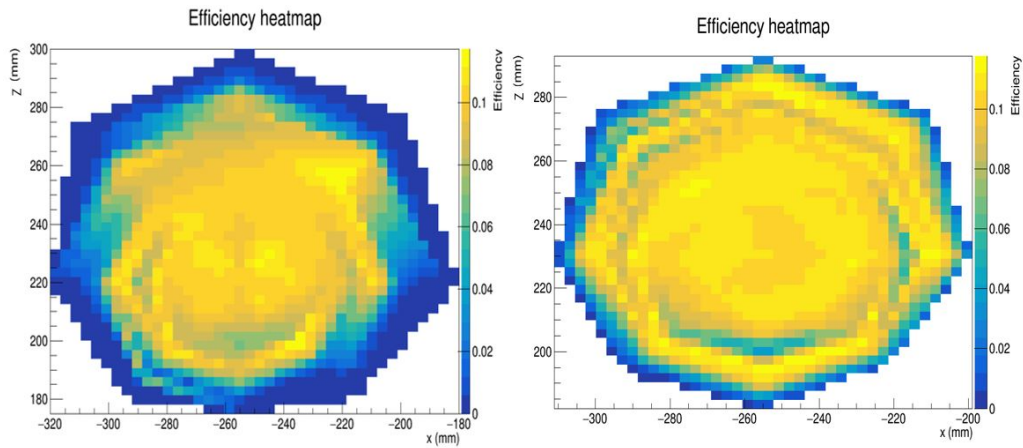


Figure 6.2: **Efficiency heat map at $\theta = 180^\circ$ (first trials)**. Left: first plot is not well defined, PMT and reflector ring are not clearly visible. Right: details around the PMT and reflector ring get improved because large statistics on data taking is considered.

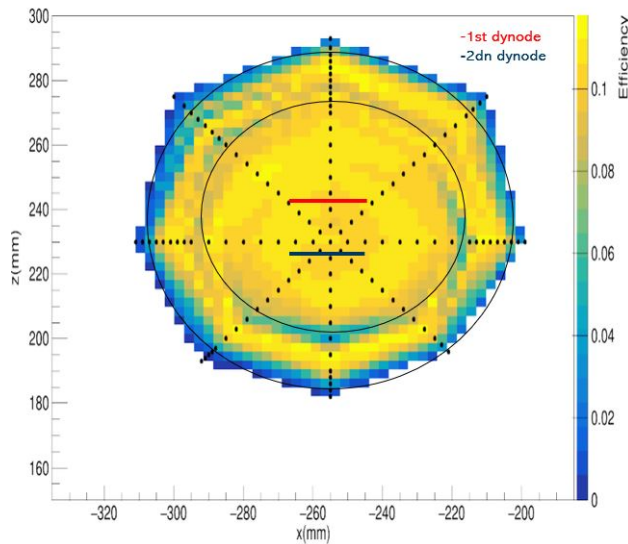


Figure 6.3: **Efficiency heat map at $\theta = 180^\circ$ (optimized by interpolation)**. The diagonals data points are illustrated, the plot also shows the optimized linear interpolated result. The inner ring represents the PMT and the outer ring the edge of the reflector ring.

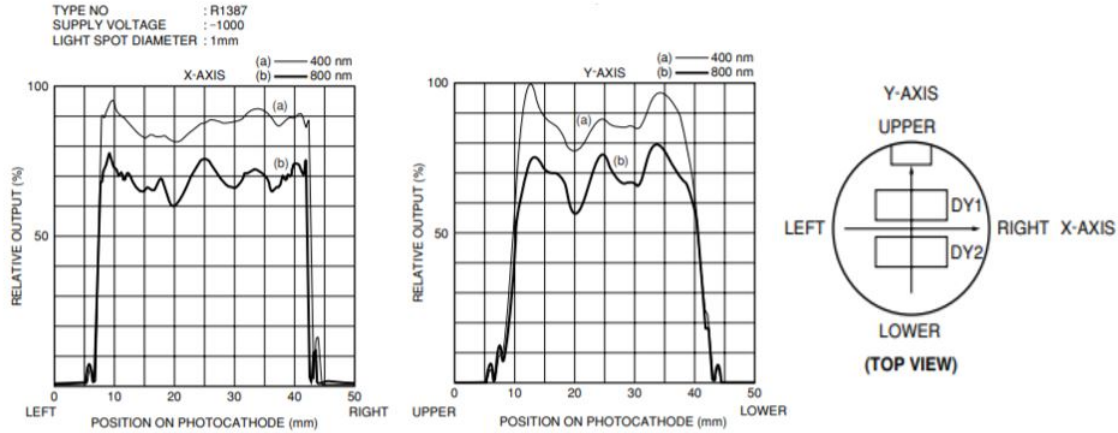


Figure 6.4: **Relative output of the Hamamatsu PMT.**³² Left-Center. Two plots of the relative output of a PMT, where the horizontal and vertical axis of the photocathode were scanned with different wavelengths. Right: Top view of a Hamamatsu PMT, first and second dynode are seen with reference lines for scanning at x-y axis.

relation is important to understand the behaviour of PMTs and the results discussed above. Furthermore, there are other experiments as IceCube³⁸ and Hyper-Kamiokande³⁹ that also using Hamamatsu PMTs as photodetectors, observed some similar patterns with analysis of gain variation, relative efficiency, uniformity and time responses. Hyper-Kamiokande concluded that PMTs have non-uniform charge, time responses and Photo Detection Efficiency (PDE) along large photocathode area.³⁹ On the other hand, IceCube study suggests that photoelectron trajectories are different when arrived at the first dynode, affecting the production of secondary electrons, this is directly related with variations in gain depending on the direction of the incidence of the photon.³⁸ Preliminary conclusions on this work for KM3NeT PMTs are compatible with the results observed by IceCube and Hyper-Kamiokande. Such non-uniformity of PMT responses need to be understood and as requirement to build a better model of PMT response, thus being implemented in the detector simulation.

Figure 6.6 shows a comparison for the Hamamatsu R12199-2 PMT: the blue line is data from ECAP laboratory (also KM3NeT collaborator)⁴⁰ which provides data of DE with associated errors, the black line is the data of the PMT region taken from Figure 6.5, without errors bars due to the incident reported in Section 6.6. Data points of the PMT region in Figure 6.5 are between [-275,-195] mm, resulting in 80 mm in 9 data points. In order to compare data point at the origin, a shift of $x = +235$ mm is applied in Figure 6.6. Figure 6.6a shows higher values of efficiency for ECAP data regarding Nikhef (this work) where subtraction of background was performed (see Section 5.1.3). Furthermore, ECAP data were taken with different setups and experimental conditions (PMT is not inside the DOM without mimic the environment). On the other hand, Figure 6.6b compares both data set, by applying a scale factor (2.2) looking to better compare their conclusions about the photocathode asymmetry effect on the DE. Both results seem to point the

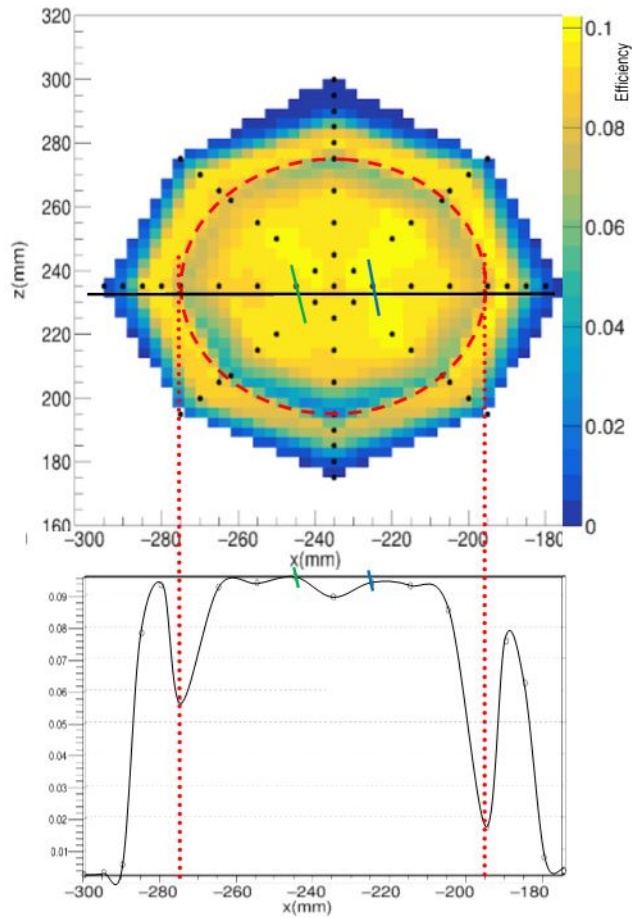


Figure 6.5: **Projection of efficiency points.** Top: PMT scanning at 180° , different PMT of the same DOM, dynodes position represented the first dynode in blue and second dynode in green. Black line represents points projected in the efficiency plot and red dashed lines the edge between the PMT and reflector ring. Bottom: projection plot of efficiency at 180° for the PMT at x position.

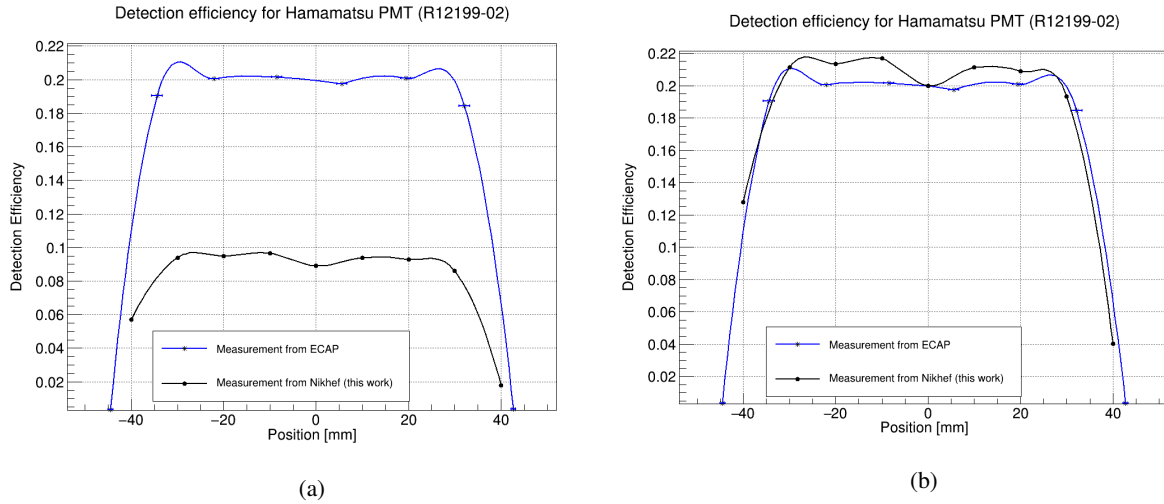


Figure 6.6: **Detection Efficiency for the Hamamatsu PMT.** a) Comparison between PMT efficiency measurements taken from Erlangen⁴⁰ and Nikhef (this work). b) Data from Nikhef scaled by a factor of 2.2 and compared with Erlangen data.

same conclusion about the asymmetry effect of the photocathode affecting the shape of the DE along the PMT. The interesting part around origin shows how both lines have a significant change in efficiency, supposed to be affected by the dynode position as discussed before. Moreover, the factor 2.2 may represent a convolute effect of physics (as the propagation medium, air in ECAP, water in Nikhef) and others experimental conditions (single PMT in ECAP, PMT embedded in the DOM in Nikhef).

6.1.2 PMT Scanning: 150° laser-PMT

The DOM was rotated 30° in the horizontal plane regarding initial setup. Figure 6.7 shows the displacement and the new view of the PMT from the laser line of sight, it is the same PMT used in the first scanning (Figure 6.1).

Figure 6.8 shows the four diagonals and the interpolated efficiency heat map. It is visible that on the right side has a relative higher efficiency. The reflector ring separation is visible on the top and bottom of the plot, but it is not easy to differentiate this from the left to right side.

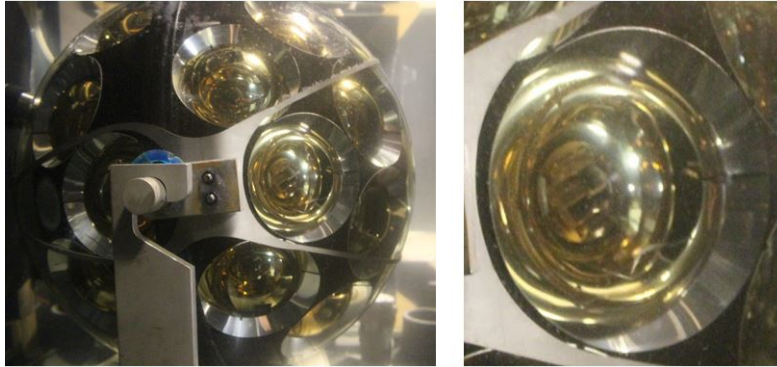


Figure 6.7: **Location of the DOM at 150°** . Left: picture of the whole DOM inside the aquarium 30° rotated. Right: view from the line of sight of the laser. The angle between the laser and the optical axis is 150° .

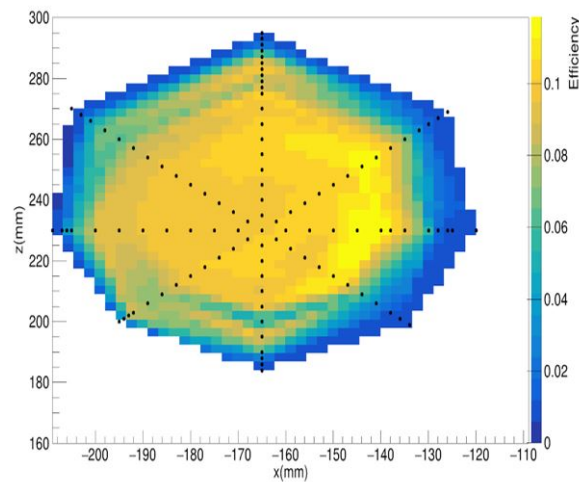


Figure 6.8: **Efficiency heat map at $\theta = 150^\circ$ (optimized by interpolation)**. Diagonals data points are illustrated, the plot also shows the optimized linear interpolated result. The efficiency is relatively higher on the right side at $(-140, 235)$ position, the separation of the reflector ring is not clear enough.

6.1.3 PMT Scanning: 120° laser-PMT

The DOM was rotated another 30° in the horizontal plane regarding previous setup. Figure 6.9 shows the frontal view of the new rotation. The vertical support starting to blocks the view of PMT from the laser.

The same methodology was repeated as before, the heat map obtained in this case is shown in Figure 6.10:

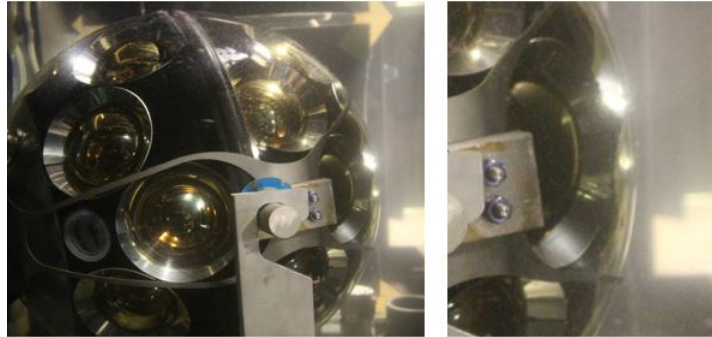


Figure 6.9: **Location of the DOM at 120° .** Left: picture of the whole DOM inside the aquarium rotated another 30° . Right: view from the line of sight of the laser. Now the angle between the laser and the optical axis is 120° . The vertical supports starts to block the PMT.

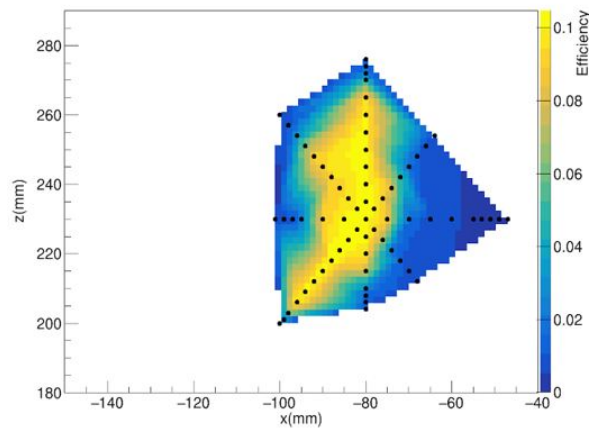


Figure 6.10: **Efficiency heat map at $\theta = 120^\circ$ (optimized by interpolation).** Diagonals data points are illustrated showing the linear interpolated result. The efficiency is relative higher on the vertical diagonal, and the separation of the reflector ring is not clear. The influence of the vertical support is seen as blocking the view of the PMT.

6.1.4 PMT Scanning: 90° laser-PMT

The DOM was rotated another 30° in the horizontal plane regarding latest setup. Figure 6.11 shows the view from the laser line of sight. The PMT is now totally blocked by the vertical support.

Even with the obstruction the data taking proceed anyway. In this case it was impossible to scan with four diagonals, instead of that, vertical and horizontal scanning were performed. The heat map as result is presented in Figure 6.12. The relative efficiencies reach $\sim 10^{-3}$ due to the evident obstruction of the PMT by the vertical support blocking the

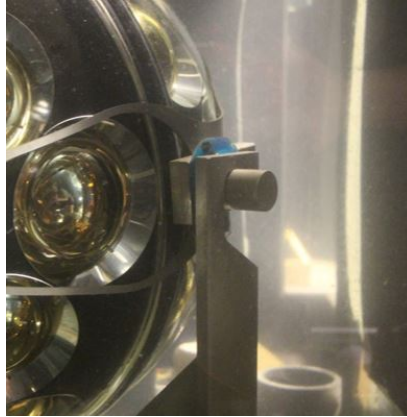


Figure 6.11: **Location of the DOM at 90°** . Picture of the whole DOM inside the aquarium rotated another 30° . Now the angle between the PMT and the laser is 90° . The view of the PMT from the laser is totally blocked by the vertical support.

photons to the PMT, representing noise for our data.

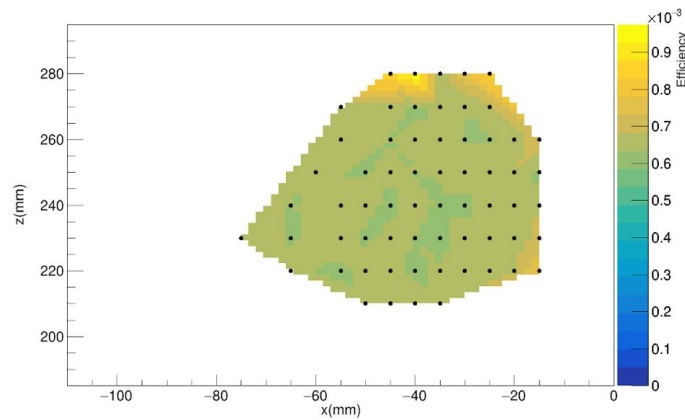


Figure 6.12: **Efficiency heat map at $\theta = 90^\circ$ (optimized by interpolation)**. Diagonals data points are illustrated showing the linear interpolated result. The efficiency is relative "higher" on the vertical diagonal, and the separation of the reflector ring is not clear. The vertical support was totally blocking the view of the PMT.

6.2 Symmetry response on light detection efficiency

Figure 6.13 shows a plot of relative acceptance (normalized angular dependence) vs $\cos(\theta)$ (from -1 to 0.2 from scanning plots at $\theta = [180, 150, 120, 90]$). Each heat map (optimized by interpolation) was integrated over the scanned

surface of the PMT, in order to obtain a normalised result, and plotted against $\cos(\theta)$. In this sense, data are compared with the latest OMGSim Monte Carlo for the angular acceptance of the DOM in KM3NeT. The angular dependence of the PMT effective area is thus called angular acceptance, and quantifies the DE at different angles of light incidence. The Monte Carlo gives an average efficiency at several angles, and this experimental research estimates four of them in the same way. Monte Carlo includes the complex structure of glass, silicone gel, handcrafted PMTs and reflector rings. The simulation is based on photons passing through seawater and this experimental research used tap water.

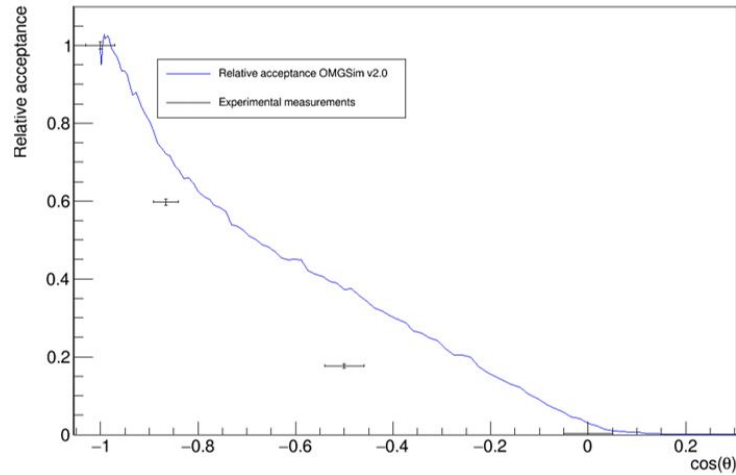


Figure 6.13: **Relative acceptance vs $\cos(\theta)$ for a KM3NeT DOM.** The experimental measurements shown are obtained from each heat map (optimized by interpolation) and integrating over the scanned surface obtaining a normalised relative acceptance plot. The blue line corresponds to the latest KM3NeT OMGSim v2.0 Monte Carlo.

All the data collected and summarized in the last section was plot over official results from OMGSim 2.0, looking to find the level of Data/Monte Carlo agreement in this work. The first data point at $\cos(\theta) = -1$ corresponds when the optical axis with the laser and the PMT is 180° . For angles, $\theta = [120^\circ, 90^\circ]$ ($\cos \theta = [-0.5, 0]$) the vertical obstruction can be a reason for the less efficiency compared with expectations. An interesting point is that for $\theta = 150^\circ$, efficiency is in turn lesser than expected, however this efficiency heat map was not affected by the vertical obstruction. In this case, it seems necessary to perform an enhanced data taking routines to other PMTs, looking to compare and validate the Data/MC agreement. Data obtained in this study is well below predictions.

6.3 Symmetry scanning results

In this section, the same experimental setup was used but with another PMT choice in order to avoid the problem of the vertical obstruction. Scanning at opposite angles were performed aiming to find some symmetries/asymmetries

for the PMT response. Using the scheme presented in Figure 5.8 measurements at $\theta = [210^\circ, 180^\circ, 150^\circ]$ were carried out. Figure 6.14 shows the heat map results.

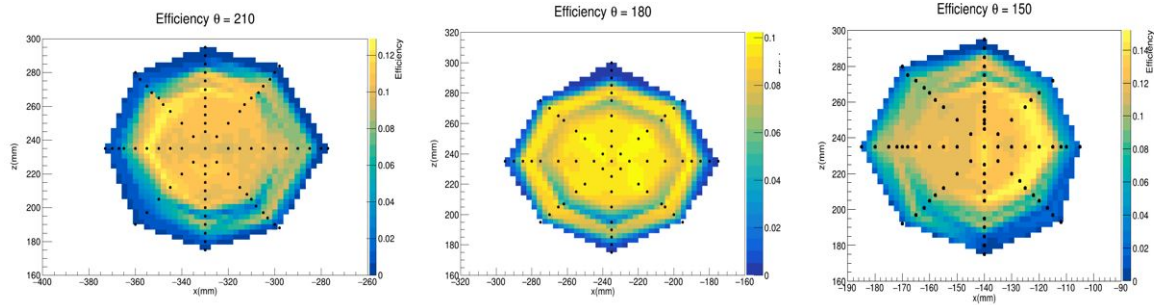


Figure 6.14: **Efficiency scanning plots used to study symmetries in PMTs (optimized by interpolation).** The plots compare the heat maps at 3 different angles. When the PMT is fixed at $\theta = 180^\circ$, next angles are rotating 30° to right and 30° to left, as a mirror-like projection.

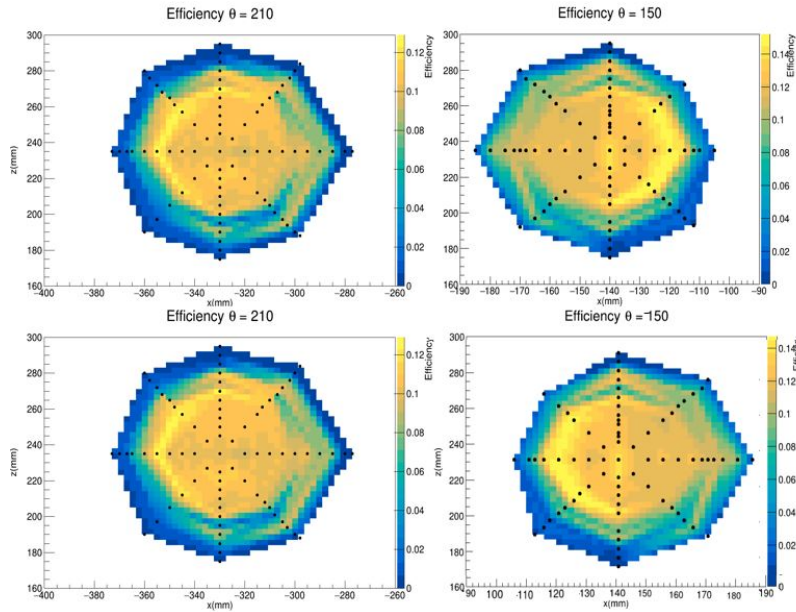


Figure 6.15: **Symmetry relations between heat maps (optimized by interpolation).** Two heat maps on the top are for $\theta = [210^\circ, 150^\circ]$. In order to compare the heat maps at 150° the x coordinates were flipped and the heat map for $\theta = 210^\circ$ is kept without flipping.

Figure 6.15 shows the relation between the above heat maps. It is important to remark that because scales plots are not directly comparable. Still, primarily the color blue represents less efficiency and yellow high efficiency, taking as reference the color scale of the efficiency plot at $\theta = 150^\circ$. Plots on the first column represent the heat map of the PMT at $\theta = 210^\circ$, while the plots on the second column belong to the PMT at $\theta = 150^\circ$. The differences appear in the second row, in which the plot at $\theta = 150^\circ$ was flipped (shifted in x), in order to obtain a mirror-like effect. When the DOM is at $\theta = 180^\circ$, and it is rotated 30° to the left side ($\theta = 210^\circ$), the expected behaviour should be the same when rotated 30° to the right ($\theta = 150^\circ$). In this reasoning, both plots in the second row, should be therefore compatible, but taking into account the corresponding uncertainties. Being aware of that, the photo-sensible region of the PMT seems to show a comparable pattern of efficiency. The PMT would keep certain symmetry on detection of light at opposite angles. Although, after flipping efficiencies as a suggested method for equivalence, one of the heat maps present a higher efficiency range; they might be related by the non-uniformity of the photocathode and the positions of the dynode and effects of the reflector ring of the DOM.

6.4 Timing information: ToT distribution

Each data point for efficiency heat maps additionally record valuable data as timing information of the events. When taking 60 seconds of data point measurements, the ToT and arrival time distributions are also stored. Each point of measurements has a ToT distribution recorded with all the hits from the laser. The ToT distribution peak is at 26.4 ns for a single photoelectron (spe), as used for calibration purposes. Figure 6.16 shows three different ToT distributions recorded for a PMT as presented by the scheme in Figure 5.8. ToT peak distribution is affected by the incident photons in different directions. The steep slope for $\text{ToT} > 26.5$ ns suggests that the measurements are in the spe regime as calibration requirement (26.4 ns for spe). ToT distribution is impacted by the non-homogeneity of the PMT surface and the arrival time of the hits flashed by the laser are also affected. This result needs to be further checked with other PMTs and improved data taking routines, and they are only presented in this work to infer about the behaviour of ToT distribution in PMTs. Without enough statistical data (Section 6.6) is difficult to conclude the analysis, more than an apparent loss of resolution in the ToT, nonetheless, slightly compatible with conclusions extracted from PMT studies in IceCube and Hyper-Kamiokande.^{38 39}

6.5 Timing information: arrival time distribution

In the same way as for ToT, the arrival time distribution of photons is stored. Figure 6.17 shows time distributions peak between [220, 221] ns, the moment when the most of incoming photon arrives, at right the corresponding heat map shows detection delayed in the PMT, slightly consistent. The black line distribution shows a small shifted peak. Comparing that result with the heat map, it is only few ns differing with the color scale. The laser timing was kept constant, but the position of incidence was varied.

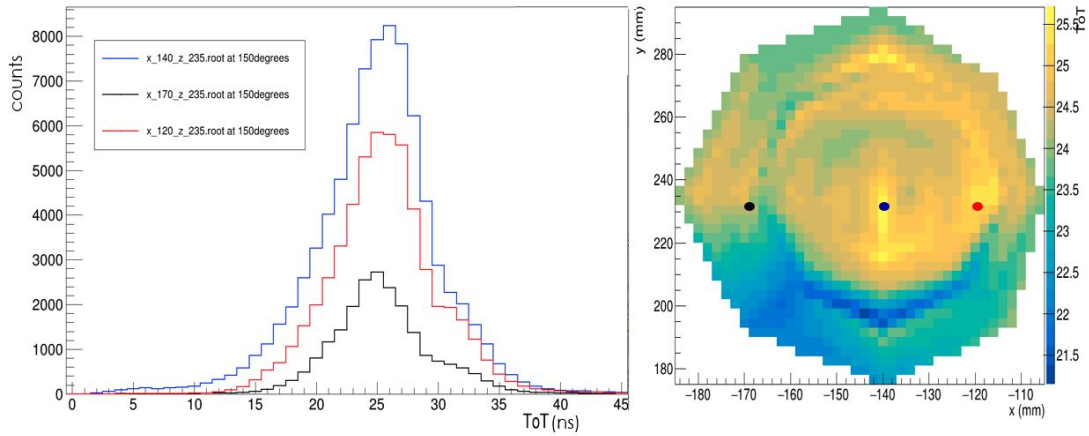


Figure 6.16: **ToT distributions of three different points in the PMT.** Left: ToT distribution comparison, at different position. Right: Corresponding heat map of the ToT distribution in the PMT shows three color points represented in the distribution at left.

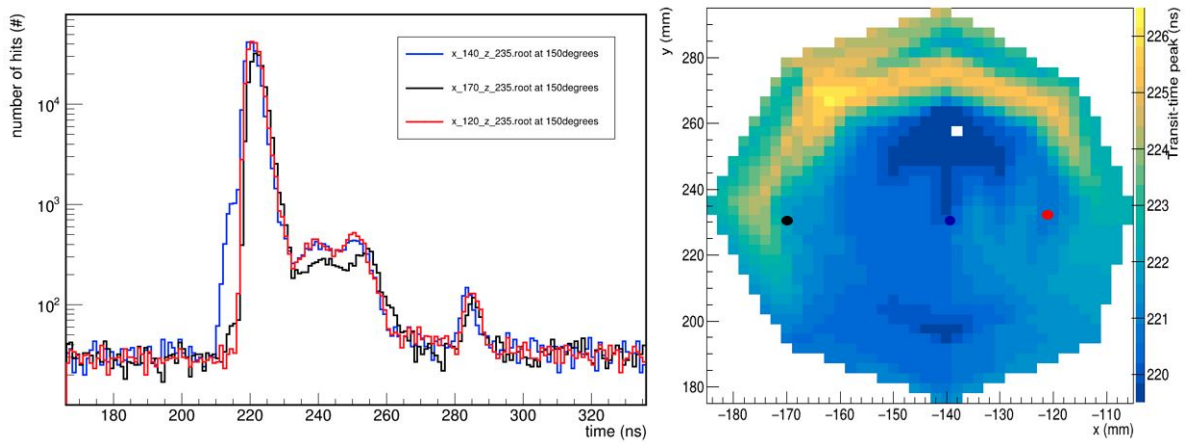


Figure 6.17: **Arrival time distribution and heat map for PMTs.** Left: three points in the PMT were studied through the arrival time distribution. Right: heat map for arrival time distribution. The range of arrival time distribution goes from [220, 226] ns in the PMT.

Before the main peak at 220 ns there is a small population identified as prepulses. Those pulses are produced by photons releasing electrons on the first dynode, and these photons pass through the photocathode without interactions.⁴¹ They are detected as the response of the PMT to a light event, but they appear before the typical arrival time of the main pulse. After the main peak (220 ns) there are seen some delayed pulses. These pulses appear after the typical transit time of the PMT, they form a peak that follows the main pulses in a transit time distribution. These peaks are the result by elastic scattering photoelectrons on the first dynode without liberating any secondary electrons. After accelerated again towards the first dynode, they may start a regular multiplication process with the final pulse arriving later than regular pulses. Finally, in order to see more visual differences, other points in the surface must be compared, but again, incident reported in Section 6.6 limit the possibility of validate and extend such conclusions in this work.

6.6 Data availability and reproducibility issues

This section is very important to mention due to the fact that the measurement data that is presented was accidentally deleted by a human error. The backup routines were not running unfortunately neither in the computing centre on that date. Fortunately, all the plots shown were saved in a presentation, and they are shown as results of this thesis, and regularly presented in our internal groups meeting. The problem was that a huge amount ~ 1000 of data files became unavailable. It implied around four months of recovery and data repairing activities. First, experts at Nikhef laboratory helped with a text document that contains recovery files with names like "f000000000.root", directories with ~ 5000 recovery data and corrupt files. It was not an easy work of classification of data. The next problem was that most of the recovery files were broken. Each point scanned at the PMT contained information from 31 channels (PMT) that were needed for symmetry analysis. A classification code was developed by Juan David Alcivar and Genesis Mendoza to find good root files. Even ~ 100 root files were not broken, they are like a ghost, again too much difficult to know at which point the file belongs. When a file was saved, for simplicity the format name was $x_000_z_000.root$ that represents the position of the scanned point. It was an interesting lesson and hard to accepted, but humans errors occur anytime, specially at the laboratory.

Chapter 7

Conclusions and Future Work

This thesis aimed to study the performance on light Detection Efficiency in KM3NeT DOMs. For fulfilling objectives, two types of analysis were developed: PMT scanning at different angles (heat maps for efficiency) and symmetry studies for PMT DOM response. This experimental research was developed at Nikhef laboratory in Amsterdam.

The first analysis allowed to conclude the pertinence of the PMT scanning technique for DE estimation. Two outcomes can be extracted: 1) Photocathode asymmetry has an appreciable influence in the DE, also see in other experiments using Hamamatsu PMT. The effect is well understood and inputs of this work are very helpful towards an absolute angular acceptance response. 2) There is a strong evidence that DOM design perfectly responds to light source emission from several directions of photon incidence. Symmetry patterns seems to be reproducible at a better resolution for extended an improved data.

The two set of measurements as useful data requires to be validated in order to built better models for PMT detection efficiency, as well the DOM response and symmetry patterns on light detection. This experimental research was a challenge when a human mistake deleted all the data from the results. It gave the possibility to improve programming skills. The deleted data was filtered for recovery and extract valuable information.

Finally, this research gives important inputs for KM3NeT and Ecuador. In Ecuador, the development of front-line technologies and training on photonics test bench are very delayed. It gives the possibility to start a modest laboratory in Yachay Tech on PMTs technology that could be used in a wide range of research areas. As an improvement for future work optimization, the measurements performed at Nikhef laboratory test bench might be automated, in order to spend less time on data taking. Moreover, the joint compromise about rules of safety and good practices at the place of work, as double-checking of backup routines on local computing centres.

Bibliography

- [1] Milan M Ćirković and Slobodan Perović. Alternative explanations of the cosmic microwave background: A historical and an epistemological perspective. *Studies in History and Philosophy of Science Part B: Studies in History and Philosophy of Modern Physics*, 62:1–18, 2018.
- [2] KM3NeT .
- [3] Franco Ferrari and Ewa Szuszkiewicz. Cosmic ray recipes. *arXiv preprint astro-ph/0601158*, 2006.
- [4] Thomas K Gaisser, Ralph Engel, and Elisa Resconi. *Cosmic rays and particle physics*. Cambridge University Press, 2016.
- [5] Yoon, YS, Ahn, HS, Allison, PS, Bagliesi, MG, Beatty, JJ, Bigongiari, G, Boyle, PJ, Childers, JT, Conklin, NB, Coutu, S, et al. Cosmic-ray proton and helium spectra from the first cream flight. *The Astrophysical Journal*, 728(2):122, 2011.
- [6] S Ahmad, D Allard, M Ambrosio, L Anchordoqui, A Anzalone, Y Arai, C Aramo, K Asano, M Ave, P Barrillon, et al. An evaluation of the exposure in nadir observation of the jem-euso mission. 2013.
- [7] Vladimir Ptuskin, Svetlana Rogovaya, and Vladimir Zirakashvili. On ultra-high energy cosmic rays: origin in agn jets and transport in expanding universe. *Advances in Space Research*, 51(2):315–321, 2013.
- [8] Wolfgang Pauli. *Collected Scientific Papers: By Wolfgang Pauli... Edited by R. Kronig and VF Weisskopf*. London, Sydney, 1964.
- [9] CL Cowan, FB Harrison, AD McGuire, F Reines, and HW Kruse. Detection of the free neutrino: A confirmation. *Camb. Monogr. Part. Phys. Nucl. Phys. Cosmol.*, 14:38–42, 2000.
- [10] Gaillard Danby, JM Gaillard, Konstantin Goulianos, LM Lederman, N Mistry, M Schwartz, and J Steinberger. Observation of high-energy neutrino reactions and the existence of two kinds of neutrinos. *Physical Review Letters*, 9(1):36, 1962.
- [11] K Kodama, N Ushida, C Andreopoulos, N Saoulidou, G Tzanakos, P Yager, B Baller, D Boehnlein, Walter Freeman, B Lundberg, et al. Observation of tau neutrino interactions. *Physics Letters B*, 504(3):218–224, 2001.

- [12] Kamiokande Collaboration et al. Evidence for oscillation of atmospheric neutrinos. *arXiv preprint hep-ex/9807003*, 1998.
- [13] JL Hewett, H Weerts, R Brock, JN Butler, BCK Casey, J Collar, A de Gouvea, R Essig, Y Grossman, W Haxton, et al. Fundamental physics at the intensity frontier. *arXiv preprint arXiv:1205.2671*, 2012.
- [14] Guido Fantini, Andrea Gallo Rosso, Francesco Vissani, and Vanessa Zema. The formalism of neutrino oscillations: an introduction. *arXiv preprint arXiv:1802.05781*, 2018.
- [15] Bruno Pontecorvo. Neutrino experiments and the problem of conservation of leptonic charge. *Sov. Phys. JETP*, 26(984-988):165, 1968.
- [16] Ziro Maki, Masami Nakagawa, and Shoichi Sakata. Remarks on the unified model of elementary particles. *Progress of Theoretical Physics*, 28(5):870–880, 1962.
- [17] Keith A Olive, Kaustubh Agashe, Claude Amsler, Mario Antonelli, Jean-Francois Arguin, David M Asner, H Baer, Henry R Band, RM Barnett, Tullio Basaglia, et al. Review of particle physics. *Chinese physics C*, 38(9):090001, 2014.
- [18] André de Gouvêa, K Pitts, K Scholberg, GP Zeller, J Alonso, A Bernstein, M Bishai, S Elliott, K Heeger, K Hoffman, et al. Neutrinos. *arXiv preprint arXiv:1310.4340*, 2013.
- [19] J Abraham, P Abreu, M Aglietta, C Aguirre, D Allard, I Allekotte, J Allen, P Allison, J Alvarez-Muñiz, M Ambrosio, et al. Correlation of the highest-energy cosmic rays with the positions of nearby active galactic nuclei. *Astroparticle Physics*, 29(3):188–204, 2008.
- [20] Eli Waxman and John Bahcall. High energy neutrinos from astrophysical sources: An upper bound. *Physical Review D*, 59(2):023002, 1998.
- [21] Abraham Loeb and Eli Waxman. The cumulative background of high energy neutrinos from starburst galaxies. *Journal of Cosmology and Astroparticle Physics*, 2006(05):003, 2006.
- [22] Silvia Adrián-Martínez, M Ageron, F Aharonian, S Aiello, A Albert, F Ameli, E Anassontzis, M Andre, G Androulakis, M Anghinolfi, et al. Letter of intent for km³net 2.0. *Journal of Physics G: Nuclear and Particle Physics*, 43(8):084001, 2016.
- [23] Mark Thomson. *Modern particle physics*. Cambridge University Press, 2013.
- [24] David JL Bailey. The effect of the group velocity and dispersion on photon arrival times in the antares detector. *ANTARES-Phys/2001-005*, 2001.
- [25] HAROLD Yepes-Ramírez, ANTARES Collaboration, et al. Characterization of optical properties of the site of the antares neutrino telescope. *Nuclear Instruments and Methods in Physics Research Section A: Accelerators, Spectrometers, Detectors and Associated Equipment*, 725:203–206, 2013.

- [26] Claudio Kopper, Representing the KM3NeT Consortium, et al. Performance studies for the km3net neutrino telescope. *Nuclear Instruments and Methods in Physics Research Section A: Accelerators, Spectrometers, Detectors and Associated Equipment*, 692:188–191, 2012.
- [27] P Bagley, P Werneke, F Fehr, J Perkin, EC Marcoulaki, M Battaglieri, F Colijn, A Grimaldi, Z Guede, D Real, et al. Km3net: Technical design report for a deep-sea research infrastructure in the mediterranean sea incorporating a very large volume neutrino telescope. 2009.
- [28] R Bruijn and Daan van Eijk. The km3net multi-pmt digital optical module. In *The 34th International Cosmic Ray Conference*, volume 236, page 1157. SISSA Medialab, 2016.
- [29] Ronald Bruijn. The km3net digital optical module and detection unit. In *EPJ Web Conf.*, volume 207, page 06002, 2019.
- [30] Karlijn Kruiswijk et al. Bioluminescence at the km3net neutrino telescope. B.S. thesis, 2019.
- [31] Alan Migdall, Sergey V Polyakov, Jingyun Fan, and Joshua C Bienfang. *Single-photon generation and detection: physics and applications*, volume 45. Academic Press, 2013.
- [32] Hamamatsu Photonics. Photomultiplier tubes: Basics and applications. *Edition 3a*, 310, 2007.
- [33] S Aiello, SE Akrame, F Ameli, EG Anassontzis, M Andre, G Androulakis, M Anghinolfi, G Anton, M Ardid, J Aublin, et al. Characterisation of the hamamatsu photomultipliers for the km3net neutrino telescope. *Journal of Instrumentation*, 13(05):P05035, 2018.
- [34] KM3NeT Collaboration et al. Expansion cone for the 3-inch pmts of the km3net optical modules. *Journal of Instrumentation*, 8(03):T03006, 2013.
- [35] Photomultiplier Tubes. Assemblies for scintillation counting & high energy physics. *Hamamatsu Co., Hamamatsu, Japan*, 2012.
- [36] M Lipiński, E Van Der Bij, J Serrano, T Włostowski, G Daniluk, A Wujek, M Rizzi, and D Lampridis. White rabbit applications and enhancements. In *2018 IEEE International Symposium on Precision Clock Synchronization for Measurement, Control, and Communication (ISPCS)*, pages 1–7. IEEE, 2018.
- [37] K Stankov. Alphalas gmbh gottingen. *private communication*, 2002.
- [38] Rasha Abbasi, Yasser Abdou, T Abu-Zayyad, J Adams, JA Aguilar, M Ahlers, K Andeen, J Auffenberg, X Bai, M Baker, et al. Calibration and characterization of the icecube photomultiplier tube. *Nuclear Instruments and Methods in Physics Research Section A: Accelerators, Spectrometers, Detectors and Associated Equipment*, 618(1-3):139–152, 2010.
- [39] Ke Abe, I Anghel, S Playfer, O Drapier, J Kameda, SY Kim, M Barbi, C Checchia, A Kaboth, S Tobayama, et al. Hyper-kamiokande design report. Technical report, 2018.

- [40] Jonas Reubelt. *Characterisation of photomultiplier tube models to be used in the KM3NeT project*. PhD thesis, 2012.
- [41] BK Lubsandorzhiev, RV Vasiliev, YE Vyatchin, and BAJ Shaibonov. Photoelectron backscattering in vacuum phototubes. *Nuclear Instruments and Methods in Physics Research Section A: Accelerators, Spectrometers, Detectors and Associated Equipment*, 567(1):12–16, 2006.

Abbreviations

- AGNs** Active Galactic Nuclei 7, 11
ARCA Astroparticles Research with Cosmics in the Abyss 2, 13
AS Air Shower 6
- CC** Charged Current 7
CE Collection Efficiency 23, 36
CMB Cosmic Microwave Background 2
CRs Cosmic Rays 1, 2, 5–7, 10
- DE** Detection Efficiency x, 3, 23, 24, 27, 30, 31, 33, 35, 36, 38, 40, 44
DOM Digital Optical Module x, 27, 28, 31
DU Detection Unit 27
- EAS** Extensive Air Shower 6
ECRs Extragalactic Cosmic Rays 6
EE Extrem Energy 6
- GCRs** Galactic Cosmic Rays 6
GRBs Gamma Ray Bursts 7, 11
- NC** Neutral Current 7
- ORCA** Oscillation Research with Cosmics in the Abyss 2, 13
- PDE** Photo Detection Efficiency 38
PMT Photomultiplier Tube viii–x, 21–23, 27, 29, 31, 35
PMTs Photomultiplier Tubes viii, 3, 21, 22, 27, 29
PWNe Pulsar Wind Nebula 12
- QE** Quantum Efficiency 23
- SM** Standard Model 7

SNRs Supernova Remnants 7, 12

ToT Time-over-Treshold 24

UHE Ultra-High Energy 1, 2, 6, 10

VHE Very-High Energy 1, 2, 6

WRS White Rabbit Switch x, 31